UNIVERSITÀ DEGLI STUDI DI PADOVA

Dipartimento di Fisica e Astronomia "Galileo Galilei"

Master Degree in Physics

Final Dissertation

Particle-gamma coincidences with Agata+Euclides for study of light-ion fusion at astrophysical energies

Thesis supervisor

Prof. Giovanna Montagnoli

Thesis co-supervisor

Dr. Mirco Del Fabbro

Candidate

Alexandru Timis

Academic Year 2022/2023

Abstract

The present thesis deals with a test experiment performed at Laboratori Nazionali di Legnaro (LNL) on the reaction ^{30}Si+^{12}C (Q_{fus} = 14.11 MeV). This system has already been studied [1] a few years ago, even in that case at LNL, using the PISOLO electrostatic deflector, and fusion hindrance was observed. The test aimed to investigate the possibility of realizing fusion measurements in the nb range using a different experimental setup. In this case, the particle-gamma coincidences technique was used exploiting the combined set-up of AGATA and silicon-array EUCLIDES. With this approach, the cross-section is obtained by counting the coincidences between the charged particles evaporated from the compound nucleus and the gamma rays emitted by the evaporation residues.

The test has been realized in inverse kinematics using the XTU Tandem accelerator of Laboratori Nazionali di Legnaro (LNL) to deliver the ^{30}Si beam at two different energies; one above (47 MeV) and the other below (40 MeV) the Coulomb Barrier. The target was a ^{12}C isotopically enriched to 99,9% in mass 12. The two calculated fusion cross-sections are compared to the previous experimental results obtained with PISOLO and also with the theoretical predictions of coupled channels calculations.

The thesis is organized in the following way:

- Chapter 1 gives a general overview of the heavy-ion reactions' features listing the different approaches in their study;

- Chapter 2 describes the experimental setup involved in the test;

- Chapter 3 deals with the data analysis;

- Chapter 4 contains the summary and the conclusions.

Contents

Chapter 1

The Physical Case

1.1   Introduction

The topic of this thesis work is the study and the data analysis of the heavy-ion fusion reaction for the system ^{30}Si+^{12}C. The term heavy-ion is used to describe all the nuclei heavier than alpha-particles. These kinds of reactions are really important because they play a crucial role in the:

- production of proton-rich nuclei;

- study of high spin nuclear structure;

- synthesis of new superheavy nuclei in the proximity of the new predicted island of stability.

The fusion of two heavy ions can be described as a two-step process following the compound nucleus model proposed by Niels Bohr [2] where first there is the formation of a compound nucleus (CN) and then there is its decay. The decay can follow two different ways:

- evaporation of light particles;

- fission in the case of heavy compound nuclei.

The process finishes with the emission of gamma rays until the evaporation residue reaches the ground state.
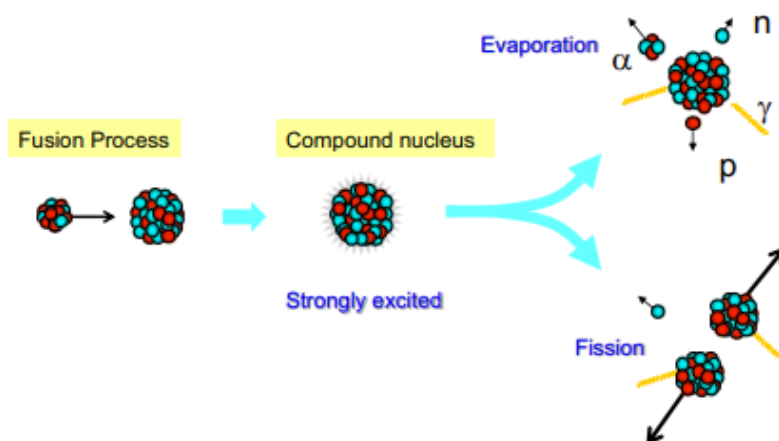

Figure 1.1: Heavy-ion fusion process: first the compound nucleus formation then its successive decay [3].

Going into more details: in the initial state there is the projectile P and the target T, a collision takes place and under certain conditions (which will be explained in the following subsection), the two nuclei become indistinguishable forming an excited compound nucleus. The projectile's nucleons suffer different collisions with the target's nucleons in such a way that all the energy is shared among all the nucleons. These several multiple collisions lead to a complete thermal equilibrium and a loss of information on the entrance channel of the system.

The compound nucleus can be considered long-lived because its formation time ($10^{-18/-19}$ s) is long if compared with the typical timescale of the direct reactions ($10^{-21/-22}$ s). From an energetic point of view the CN is formed in an excited state with an excitation energy equal to:

$$E_{ex} = Q + E_{c.m.} \tag{1.1}$$

with Q the Q-value of the reaction, whose expression is given by:

$$Q = (m_T + m_P - m_{CN,g.s.}) \, c^2 \tag{1.2}$$

and $E_{c.m.}$ is the beam energy in the center of mass frame.

For the system analyzed in this thesis, the CN is ^{42}Ca which evaporates light particles and these are measured by the array of silicon detectors EUCLIDES then the evaporation residues emit gamma rays are detected by the gamma-array spectrometer AGATA.

1.2 Subbarrier heavy-ion fusion

The simplest way to describe a heavy-ion fusion reaction is the one-dimensional potential model. With this approach, the two colliding nuclei are considered without internal structure and subjected to a potential that is composed of three different contributions:

- a long-range repulsive Coulomb potential (V_c);

- a short-range nuclear potential (V_n);

- a repulsive centrifugal potential (V_l).

The total potential (V_{Total}) is the sum of these three terms and originates a barrier, the Coulomb barrier (V_b). From a classical point of view, for energies lower than V_b, fusion is forbidden. However, the formation of the compound nucleus can take place also for energies below the Coulomb barrier. This is possible due to quantum mechanics and in particular the tunnelling effect.

Now let's describe shortly each one of these three terms.

Coulomb potential

It is the electrostatic potential among two point-like charged particles placed at a distance r. Its expression is:

$$V_c = \frac{Z_p \, Z_t \, e^2}{4 \, \pi \, \epsilon_0 \, r}, \tag{1.3}$$

where:

- e is the electric charge;

- Z_p, Z_t are the atomic numbers of the projectile and target respectively;

- ϵ_0 is the vacuum permittivity.

Eq. 1.3 is a simplified expression because it considers the two nuclei as pointless (without structure). This approximation is valid only under the condition the two nuclei do not overlap significantly. A more accurate approach is to treat the target nucleus as a sphere with a radius R and a charge Z_t, whereas the projectile is considered pointless.

With this treatment, Eq. 1.3 changes as follows:

$$V_c(r) = \frac{Z_p \, Z_t \, e^2}{4 \, \pi \, \epsilon_0} \begin{cases} \dfrac{1}{2 \, R_c} \left(3 - \dfrac{r^2}{R_c^2} \right) & \text{if} \quad r \le R_c \\[4mm] \dfrac{1}{r} & \text{if} \quad r > R_c \end{cases} \tag{1.4}$$

In the above expression, R_c is called the Coulomb radius and is equal to the sum of the radii of the two nuclei, $R_c = 1.44 \, (A_p^{1/3} + A_t^{1/3}) \, fm$.

Nuclear potential

Currently, there is no an exact expression for this term. Different empirical formulas are utilized. The most widely used is the Wood-Saxon potential:

$$V_n(r) = -\frac{V_0}{1 + exp\left(\dfrac{r - R_0}{a_0} \right)} \tag{1.5}$$

where: V_0 is the well depth, R_0 the radius and a_0 the diffuseness.
A good parametrization is the Akyuz-Winther one [5], where the values have been obtained from several elastic scattering experiments. Below is the expression for the parameters:

$$V_0 = 16 \, \pi \, \gamma \, a_0 \, \frac{R_p \, R_t}{R_p + R_t}$$

$$R_0 = R_p \, + \, R_t$$

$$a_0 = \frac{1}{1.17 \, [1 + 0.53 \, (A_p^{-1/3} + A_t^{-1/3})]}$$

$$R_t = 1.2 \, (A_t^{1/3} - 0.09) \, fm$$

$$R_p = 1.2 \, (A_t^{1/3} - 0.09) \, fm$$

$$\gamma = 0.95 \left[1 - 1.8 \, (A_p - 2 \, Z_p) \, (A_t - 2 \, Z_t) \left(\frac{A_p}{A_t} \right) \right]$$

However, this parametrization is not appropriate for most heavy ion reactions. A possible explanation can be found in [6].
A possible alternative is using the potential given by:

$$V_{d.f.}(r) = \int d \, r_1 \int d \, r_1 \, \rho_p(r_1) \rho_{t(r_2)} \, v_{N\,N}(r_2 - r_1 - r) \tag{1.6}$$

where ρ_p and ρ_t are respectively the projectile and target densities while v_{NN} is an effective nucleon-nucleon interaction.

Centrifugal potential

This last contribution comes out when solving the Schrodinger equation in the center of mass frame, after performing the expansion of the solution in terms of spherical harmonics.
The centrifugal term is:

$$V_l = \frac{l \, (l + 1) \, \hbar^2}{2 \, \mu \, r^2} \tag{1.7}$$

where l is the angular momentum and μ[1] is the reduced mass of the system.
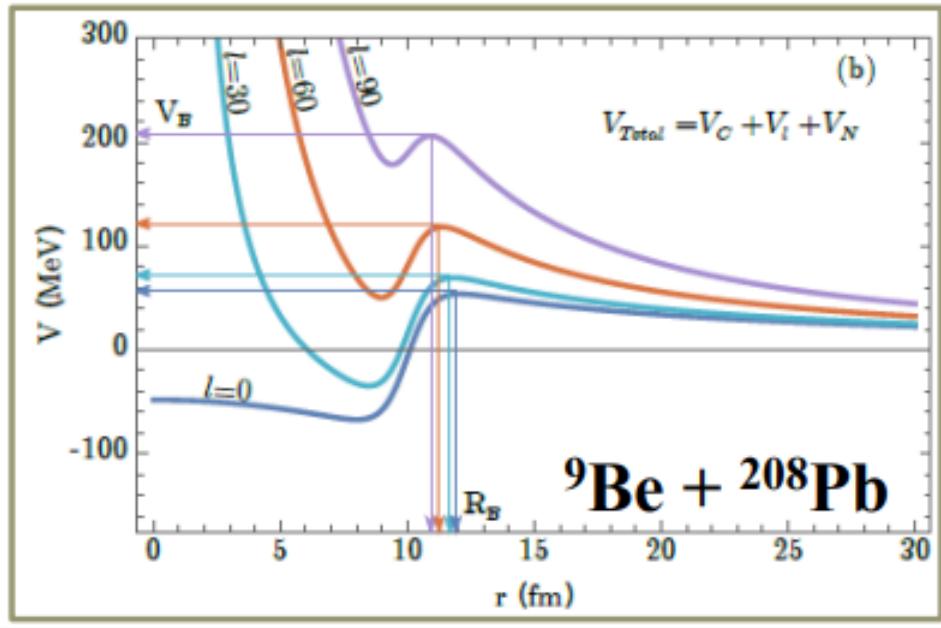
---

[1] $\mu = \dfrac{A_t \, A_p}{A_p + A_t}$

Figure 1.2: Nucleus-Nucleus potential for the system ^{9}Be+^{208}Pb for different l values [7].

In Fig. 1.2 one can see the contribution of the centrifugal barrier: it decreases the depth of the pocket and increases the height of the Coulomb barrier. These facts have important consequences on the fusion reactions.

In a simplified view, one can imagine that the formation of the compound nucleus takes place due to the presence of the potential pocket. Looking at Fig. 1.2 it is clear how increasing the angular momentum value, the pocket tends to disappear. This means that the fusion is possible up to a critical value (l_{cr}) of the angular momentum. This value is given by:

$$l_{cr} = R_b \sqrt{\frac{2\,\mu}{\hbar^2}(E_{c.m.} - V_b)} \tag{1.8}$$

where R_b and V_b are the position and respectively the height of the Coulomb barrier.

So, for angular momenta lower than l_{cr} there is the formation of the compound nucleus and then its subsequent decay by evaporation of light particles or by fission. Instead, for values of l higher than l_{cr} the contribution of the centrifugal barrier becomes important, the pocket tends to disappear and so the fusion does not take place. In such a case the two nuclei exchange nucleons during a period of contact and then separate.

Cross-section calculation

As mentioned in the abstract, this work aims to obtain a value of the fusion cross-section (σ_{fus}) for the system ^{30}Si+^{12}C at two different energies: one above and the other below the Coulomb barrier. In the next pages, a brief overview of the different approaches in order to get an expression for the σ_{fus} is given.

In the one-dimensional model, the fusion occurs if the nuclei overcome the barrier in such a way that the system is captured inside the pocket and the fusion can take place.

This implies that the fusion cross-section is linked to the probability of overcoming this barrier. This probability is expressed by the transmission coefficient $T_l(E)$. The transmission coefficient is a real number between 0 and 1. It expresses the probability that a system with angular momentum l and energy E will overcome the barrier. In particular, the value of the cross-section is proportional to this coefficient and the relation is (neglecting the spin):

$$\sigma_{fus,l} = \pi \, \lambda^2 \, (2l + 1) \, T_l(E) \tag{1.9}$$

where λ is the reduced de Broglie wavelength.

However, Eq. 1.9 is referred only to a partial wave with angular momentum l. The way to obtain the

total fusion cross-section is to sum over all the partial waves. But, as pointed out before, the fusion cannot take place for all l-values. Only the angular momenta lower than l_{cr} have a contribution to the fusion process.

This implies a formula for the total cross-section with this expression:

$$\sigma_{fus} = \sum_{l=0}^{l_{cr}} \pi \, \lambda^2 \, (2l+1) \, T_l(E) \tag{1.10}$$

Now the next step is to obtain the transmission coefficient, this is done by solving the Schrodinger equation. In such a procedure different approximations can be exploited, the most used is the Wentzel-Kramers-Brillouin(WKB) [8].

Under this approximation, the transmission coefficient is:

$$T_l(E) = \frac{1}{1 + e^{2\,\Phi}} \tag{1.11}$$

where Φ is the integral of the wave number between the two classical turning points (r_1,r_2):

$$\Phi(E) = \int_{r_1}^{r_2} k_l \, dr$$

At this point, the Hill-Wheeler approximation [9] can be used, where the Coulomb barrier is assumed to have a parabolic shape:

$$V_l(r) = V_{bl} - \frac{1}{2}\mu\,\omega_l^2 \, (r - R_{bl}) \tag{1.12}$$

where V_{bl} is the barrier height, R_{bl} the barrier position, and ω the curvature of the parabola which expression is:

$$\omega_l = \sqrt{-\frac{1}{\mu}\frac{d^2 V_l(r)}{dr^2}} \tag{1.13}$$

Within this Hill-Wheeler approximation, the transmission coefficient is [9]:

$$T_l(E) = \frac{1}{1 + exp[-\dfrac{2\pi}{\hbar\,\omega_l}(V_{bl} - E)]} \tag{1.14}$$
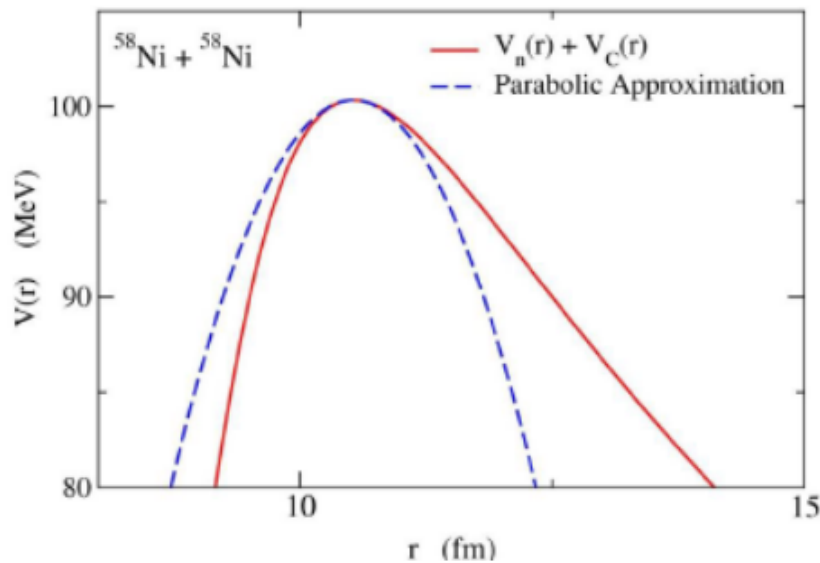

Figure 1.3: Parabolic approximation for the system ^{58}Ni+^{58}Ni [9].

This approximation is accurate in the region near the barrier and for heavy systems but shows deviations for energies below the Coulomb barrier.

Replacing Eq. 1.14 in Eq. 1.10 the total fusion cross-section can be expressed as:

$$\sigma_{fus} = \sum_{l=0}^{l_{cr}} \pi \, \lambdabar^2 \, (2l+1) \, \frac{1}{1+exp[-\frac{2\pi}{\hbar\omega}(V_{bl}-E)]} \tag{1.15}$$

In order to obtain a simpler expression, the assumption is that the curvature and the barrier height are independent of the angular momentum, and their values are the ones corresponding to the ones for the s-wave case (l = 0):

$$R_{bl} \sim R_{b0}$$

$$\omega_l \sim \omega_0$$

In this way, the expression for the transmission coefficient changes as follows:

$$T_l(E) = T_0(E) - \frac{\hbar^2 \, l(l+1)}{2 \, \mu \, R_{b0}^2} \tag{1.16}$$

The last step consists in substituting the summation with the integral and changing the variable l from l+1. This brings to the well-known Wong formula [10]:

$$\sigma_{fus}(E) = \frac{\hbar \omega_0 \, R_{b0}}{2 \, E} \, ln\left(1 + exp\left[\frac{2\pi}{\hbar\omega_0}(E - V_{b0})\right]\right) \tag{1.17}$$

In the high and low energy limits the formula has the following form:

$$\sigma_{fus}(E) = \begin{cases} \pi \, R_0^2 \left(1 - \frac{V_{b0}}{E}\right) & E \gg V_{b0} \\ \frac{\hbar\omega_0 R_{b0}}{2E} exp\left[\frac{2\pi}{\hbar\omega_0}(E - V_{b0})\right] & E \ll V_{b0} \end{cases} \tag{1.18}$$

The formula is consistent with the classical view because for $E < V_{b0}$ the cross-section is zero and also for very high energies the value tends to the geometrical cross-section ($\sigma_{geom} = \pi R_{b0}^2$): For energies below the barrier, the cross-section drops exponentially decreasing the energy. The model had great success in describing the fusion cross-section for many systems, especially the light ones.
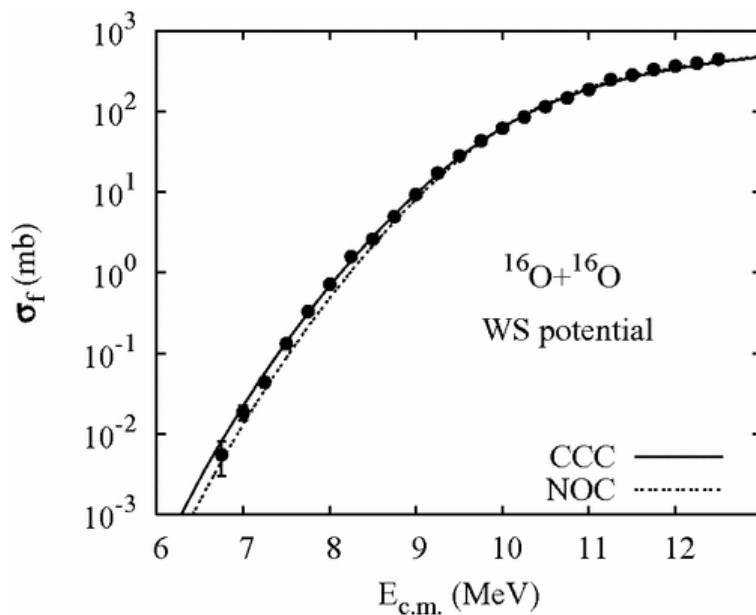

Figure 1.4: Experimental excitation function for the system ^{16}O+^{16}O compared with coupled channels calculations (solid line) and Wong's formula prediction (dashed line) [11].

The model works also for heavier systems where the nuclei are spherical and double closed-shell.
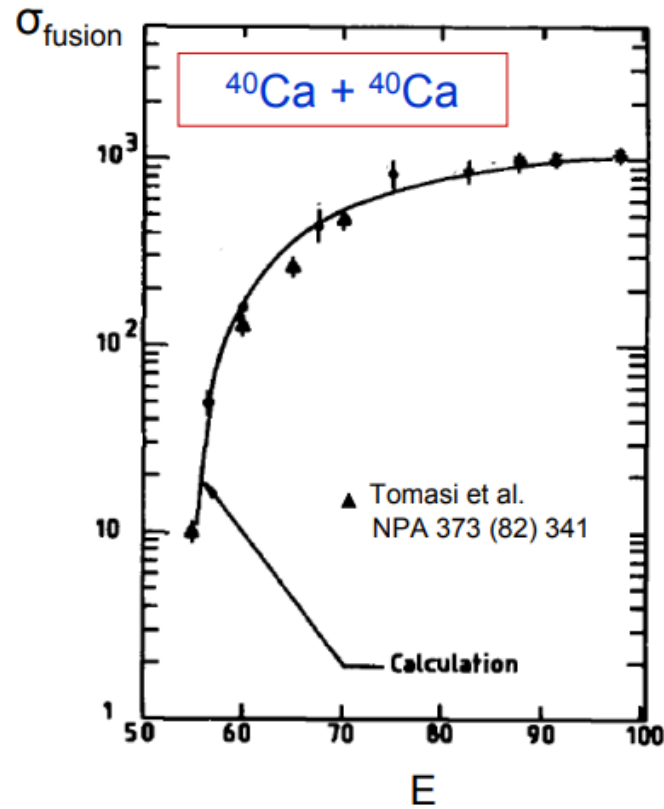

Figure 1.5: Excitation function for the reaction ^{40}Ca+^{40}Ca. The solid line indicates Wong's formula prediction [12].

However, Wong's formula does not fit the data for heavy systems in particular at sub-barrier energies where it underestimates the values as shown in the comparison in the figure below.
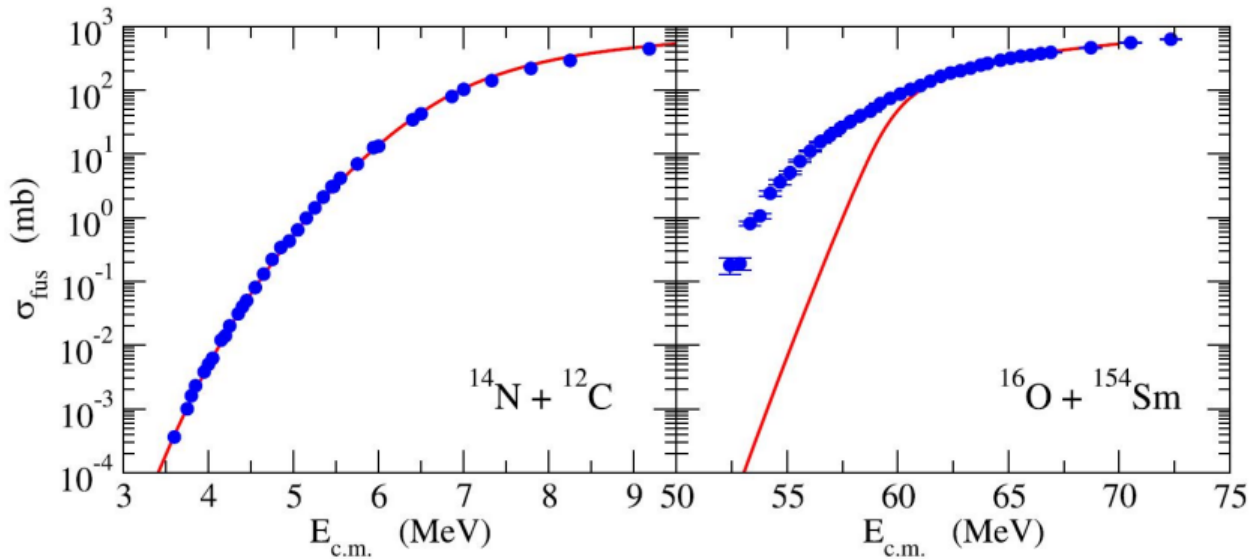

Figure 1.6: Comparison between excitation functions for the systems ^{14}N+^{12}C and ^{16}O+^{154}Sm. The red line represents the prediction of the Wong formula. The first system follows the prediction of the one-dimensional barrier model, the latter displays a large difference in energies below the Coulomb barrier [13].

Fig. 1.6 shows how decreasing the energy, the discrepancy between Wong's prediction and experimental

data increases (reaching also 2-3 orders of magnitude).
The same phenomenon is present in other systems like for example, the one analyzed in [14].
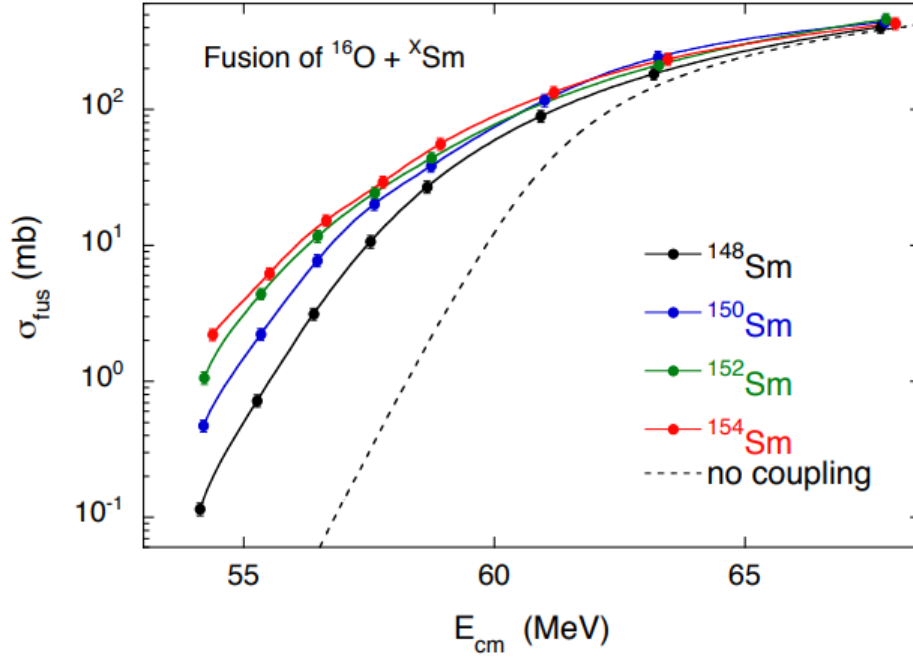

Figure 1.7: Excitation functions of ^{16}O on different Sm isotopes. The dashed line represents the estimation for the single-barrier potential model [14].

All the cross-sections are similar above the barrier, while below in all the cases, there is an enhancement with respect to the one-dimensional model. Another crucial aspect is the cross-section's difference between the systems, the explanation is in their nuclear structure. Indeed increasing the mass number the nuclei becomes more deformed.

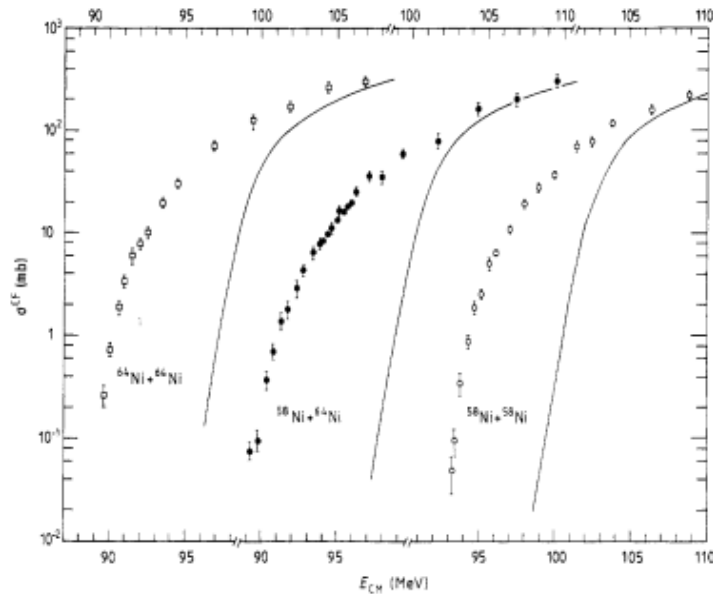A similar behavior can be observed in the excitation functions of the ^{X}Ni+^{Y}Ni systems [15].

Figure 1.8: Comparison between excitation functions of various ^{X}Ni+^{Y}Ni and the respective Wong's formula predictions (solid lines) [15].

For all three reactions, the cross-section predicted by the one-dimensional model is underestimated. Another aspect to point out is the presence of isotopic effects: the shape and the magnitude of the excitation functions for similar systems are different. Particularly, in the system ^{58}Ni+^{64}Ni the decrease of the cross-section is less steep with respect to the other two cases. A possible reason for this can be the presence of a neutron transfer channel with a positive Q-value [16].

Looking at Fig. 1.7 and Fig. 1.8 it is evident how the one-dimensional model is not accurate in reproducing the fusion cross-sections, especially for heavy systems. There is a necessity to develop a new model which has to take into account the nuclear structure of nuclei and the presence of transfer channels with positive Q-values.

Coupled-Channels model

In the one-dimensional model the only variable involved is the relative distance between the target and the projectile. However, as can be observed in Fig. 1.7 and Fig. 1.8, with this treatment there is no agreement with the experimental data. And so, it was developed the coupled channels model[17-18-19]. Within this new approach, it is necessary to consider the presence of internal degrees of freedom. In such a way the Hamiltonian of the system has the following form:

$$H_{CC} = H_k + H_0(\xi) + V_l(r) + V_{int}(r,\xi) \tag{1.19}$$

where:

- $H_k = -\dfrac{\hbar^2}{2\,\mu}\nabla^2$ is the kinetic energy;

- $H_0(\xi)$ is the intrinsic hamiltonian describing the internal structure and ξ is the variable related to the nuclear intrinsic motion;

- $V_l(r)$ is the ion-ion potential for the l-th wave and r is the relative distance between the target and the projectile;

- $V_{int}(r,\xi)$ is the coupling potential between the relative motion and the internal degrees of freedom.

The Schrodinger equation changes as follows:

$$H_{CC}\psi(r,\xi) = E(r,\xi)\psi(r,\xi) \tag{1.20}$$

Supposing the variables are separable, the total wavefunction $\psi(r,\xi)$ can be decomposed as follows:

$$\psi(r,\xi) = \sum_i \phi_i(r)\chi_i(\xi)$$

where $\chi_i(\xi)$ are the eigenfunctions and ϵ_i the eigenvalues of the intrinsic hamiltonian:

$$H_0\chi_i(\xi) = \epsilon_i\chi_i(\xi) \tag{1.21}$$

Using Dirac bra-ket notation and calling $|i\rangle$ a complete orthonormal base of the intrinsic hamiltonian, the wavefunction can be expressed as follows:

$$\psi(r,\xi) = \sum_i \phi_i(r)\,|i\rangle \tag{1.22}$$

Inserting Eq. 1.22 in Eq. 1.20 and adjusting the terms, a set of coupled equations is obtained:

$$\sum_i \left(-\frac{\hbar^2}{2\mu}\frac{d^2}{dr^2} + V_l(r) - E\right)\phi(r)\,|i\rangle = -\sum_i \left(H_0(\xi) + V_{int}(r,\xi)\right)\phi(r)\,|i\rangle \tag{1.23}$$

Exploiting the orthonormality of $|i\rangle$ and applying the bra $\langle j|$ to the previous equation, a new set of coupled equations is obtained:

$$\left(-\frac{\hbar^2}{2\mu}\frac{d^2}{dr^2} + V_l(r) - E\right)\phi_j(r) = -\sum_i M_{ji}\phi_i(r) \tag{1.24}$$

where M_{ji} is the coupling matrix whose elements are defined as follows:

$$M_{ji} = \epsilon_j\delta_{ji} + \langle j|V_{int}(r,\xi)|i\rangle \tag{1.25}$$

The matrix is symmetric and, if it is also diagonal, the solutions can be decoupled. The problem with this set of coupled equations is the large number of channels involved in the reaction. In order to diagonalize the matrix it is necessary to adopt some approximations. The system of equations can also be solved in a numerical way using some programs like for example CCFULL.

One of the most common approximations is the IWBC (Incoming Wave Boundary Condition)[20-21-22]. In this approximation, a strong absorption in the interior region is considered in such a way that the incoming flux never returns back. This is, in principle, equivalent to the effects of a deep imaginary potential acting exclusively in the inner region of the barrier [23].

A useful approximation in order to reduce the number of entrance channels and, consequently, the dimension of the coupling matrix is the iso-centrifugal approximation[24-25]. The high number of channels is due to the fact that each excited state with spin S can generate S+1 channels if it is coupled to the angular momentum l_i of the relative motion. With the iso-centrifugal approach, the orbital angular momentum is considered to be the same in all the reaction channels. In other words, the centrifugal potential is assumed to be the same for every reaction channel:

$$\frac{\hbar^2}{2\mu}\frac{l_i(l_i+1)}{r^2} \approx \frac{\hbar^2}{2\mu}\frac{J(J+1)}{r^2} \qquad \text{with } J = S + l_i \tag{1.26}$$

In this way, the coupling of the spin S with the orbital angular momentum of the relative motion is neglected. This implies the presence of only one channel for each excited state and not S+1. This brings a considerable reduction in the number of coupled channels.

Another possible approach is the sudden approximation (also called adiabatic approximation). In this case $\epsilon_i \approx 0$ because it is assumed that during the penetration of the Coulomb barrier the nuclear structure is not modified. The new elements of the coupling matrix are:

$$M_{ji} \approx \langle j|V_{int}(r,\xi)|i\rangle \tag{1.27}$$

Its validity, however, is limited only to strongly deformed nuclei [26].

At this point, factorizing the coupling potential into two terms is possible: one depending on the internal degrees of freedom and the other on the relative distance between the projectile and the target:

$$\langle j|V_{int}(r,\xi)|i\rangle = \langle j|\Lambda(r)\Gamma(\xi)|i\rangle = \Lambda(r)\langle j|\Gamma(\xi)|i\rangle \tag{1.28}$$

The next step is to consider a second approximation, named constant coupling approximation, where $\Gamma(r) = \Gamma(r_b)$ with r_b the barrier position because there the coupling is more intense. With these passages the Eq. 1.24 changes as follows:

$$\left(-\frac{\hbar^2}{2\mu}\frac{d^2}{dr^2} + V_l(r) - E\right)\phi_j(r) = -\sum_i M_{ji}\phi_i(r) = -\Lambda(r)\sum_j \Gamma_{ji}\phi_i(r) \tag{1.29}$$

These two approximations, with the use of a unitary transformation, make possible the diagonalization of the matrix.

In particular, introducing a unitary matrix U, a base of eigenfunctions $\chi_i(r)$ and the relative eigenvalues λ_i the diagonalization of the coupling matrix can be performed:

$$\sum_j U_{ji}\phi_i(r) = \chi_i(r)$$

$$\sum_{mn} U_{jm}M_{mn}U_{ni}^\dagger = \delta_{ji}\lambda_i$$

A set of decoupled differential equations of second order is obtained:

$$\left(-\frac{\hbar^2}{2\mu}\frac{d^2}{dr^2} + V_l(r) + \lambda_j F(r) - E\right)\chi_j(r) = 0 \tag{1.30}$$

Now, the problem consists in solving a set of decoupled equations where each one corresponds to the j inelastic channel and is associated with the potential $V(r) + \lambda_j F(r)$.

So, differently from the one-dimensional case where only one Coulomb barrier is present, here there is a set of barriers each one with a specific transmission coefficient.

The total transmission coefficient is given by the weighted sum of all the transmission coefficients:

$$T_l(E) = \sum_j |U_{jl}|^2 T_l(E, V(r) + \lambda_j F(r)) \tag{1.31}$$

where $|U_{jl}|^2$ is the contribution of the j-th barrier to the fusion cross-section. It can be represented by W_j and can be calculated as follows:

$$W_j = |U_{jl}|^2 = |\langle j|l\rangle|^2 \tag{1.32}$$

In this way, the total fusion cross-section is obtained as the weighted sum of the cross-section for each channel:

$$\sigma_{fus}(E) = \sum_j W_j \sigma_{j,fus}(E) \tag{1.33}$$

where $\sigma_{j,fus}$ is the fusion cross-section for the j-th channel whose expression is the following:

$$\sigma_{j,fus}(E) = \sum_l \pi\lambda^2(2l+1)T_l(E, V(r) + \lambda_j F(r)) \tag{1.34}$$

Hindrance

The hindrance, as explained before, consists in an unexpected fast decrease of σ_{fus} for extreme sub-barrier energies. This effect opposes the enhancement of fusion cross-section at low sub-barrier energies. This phenomenon was first observed in the reaction ^{60}Ni+^{89}Y. With the improvement of measurements in the $\mu b - nb$ range, was possible to observe hindrance in a lot of systems, as for example ^{64}Ni+^{64}Ni where the sharp drop-off in the fusion cross-section can be clearly seen.
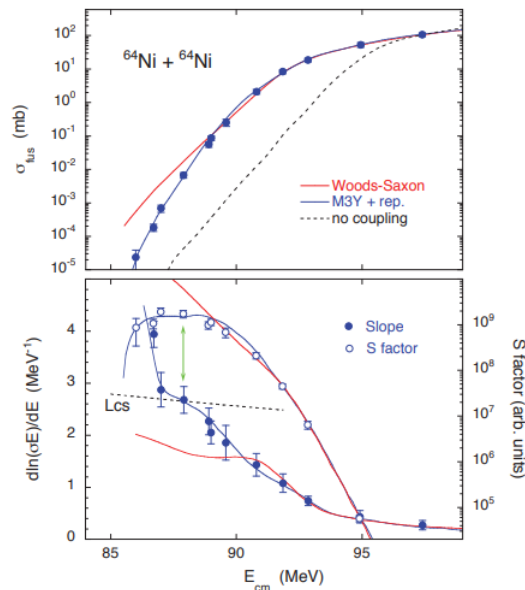

Figure 1.9: In the upper panel the excitation function for the reaction ^{64}Ni+^{64}Ni measured by Jiang et al., in the lower panel the logarithmic slope and the astrophysical S-factor [27].

From a theoretical point of view, there is not clear interpretation of the phenomenon. However, in order to explain it two models have been proposed:

- sudden approach model proposed by Misicu and Esbensen [28-29-30];

- adiabatic approach model proposed by Ichikawa et al. [31-32-33-34-35].

Both models reproduce data of several experiments.
In the sudden model, the reaction between the nuclei is assumed to happen so suddenly in such a way that the density in the overlapping region is doubled. This, due to the incompressibility of the nuclear matter, has the effect of generating a new repulsive term in the potential. The incompressibility is explained as a consequence of Pauli repulsion between nucleons. The formation of this repulsive term creates a potential that is much shallower.
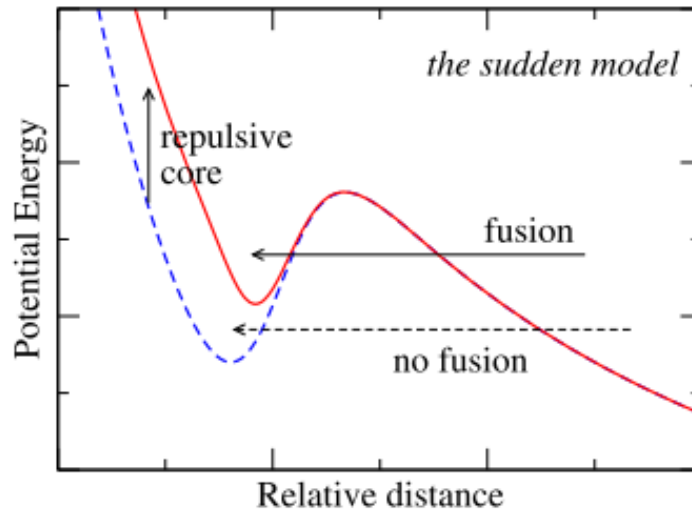

Figure 1.10: In blue the standard ion-ion potential, in red the effect of the repulsive term: the potential is much shallower with the decrease of the depth of potential's pocket at very low energies [36].

In the adiabatic model, the two nuclei are assumed to merge into a one-body potential in the overlapping region. This new potential already takes into account internal excitations. This implies an inhibition of coupling effects causing the hindrance.
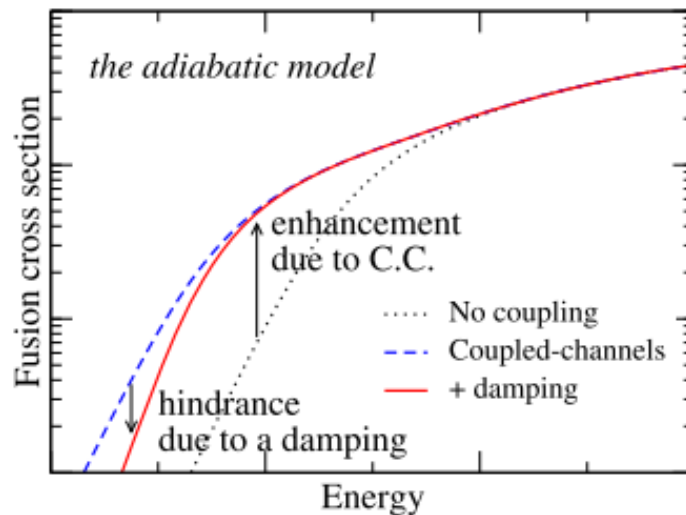

Figure 1.11: Damping in the fusion cross section due to inhibition of coupling [36].

Hindrance consists of a very rapid decrease in the fusion cross-section at deep sub-barrier energies. The decrease is much steeper than what predicted by coupled-channels calculations. So, a way to observe hindrance is by looking at the excitation function. However, depending on the system, this decrease can be more or less difficult to see. This leads to the necessity of the introducing two new quantities in order to highlight the presence of that effect.

The two quantities in question are the logarithmic slope L(E) and the astrophysical S-factor S(E) [37]. L(E) is the logarithmic derivative of the energy-weighted cross-section and represents the slope of the excitation function [38]. Its expression is:

$$L(E) = \frac{d[ln(E\sigma)]}{dE} = \frac{d(E\sigma)}{dE} \frac{1}{E\sigma} \tag{1.35}$$

The S-factor is a key quantity in the study of nuclear astrophysics reactions because it makes easier to observe the behaviour of fusion at extremely low energies. The relation is the following:

$$S(E) = E\sigma(E)exp[2\pi\,\eta] \tag{1.36}$$

where E is the energy in the center of mass frame, η the Sommerfield parameter whose definition is:

$$\eta = 0.157 \frac{Z_p Z_t}{\sqrt{\frac{E}{\mu}}} \tag{1.37}$$

with Z_p and Z_t the atomic numbers of the projectile and the target.

These two quantities are related [39], differentiating S(E) respect to energy and inserting $v = \sqrt{\frac{2E}{m}}$:

$$\frac{dS}{dE} = \left(\frac{d(E\sigma(E))}{dE} - \pi\sigma(E) \right) exp(2\pi\eta) = S(E)\left(L(E) - \frac{\pi\eta}{E} \right) \tag{1.38}$$

It is clear from Eq. 1.38 that S(E) presents a maximum for:

$$L(E) = L_{CS} = \frac{\pi\eta}{E} \tag{1.39}$$

The energy where Eq. 1.39 is verified is taken conventionally as the threshold for the hindrance. However, a distinction must be made between the reactions with positive or negative Q-values. For negative Q-values, which is the case of medium-heavy-mass systems, the energy conservation implies that $E = -Q \to S(E) = 0$ and so the maximum for S(E) is present. For $Q > 0$ systems the maximum of S(E) is not necessarily present, this makes more difficult to predict if and where the hindrance takes place. However, several experiments have indicated the presence of hindrance for reactions with a positive Q-value.

Fig. 1.9 is a confirmation of the typical behavior of a system with a negative Q-value (^{64}Ni+^{64}Ni has a Q-value of -48.8 MeV). In the lower panel, the S-factor clearly displays the presence of a maximum and in correspondence with this energy, the experimental fusion cross-section starts to fall steeper with respect to a standard coupled channels calculation.

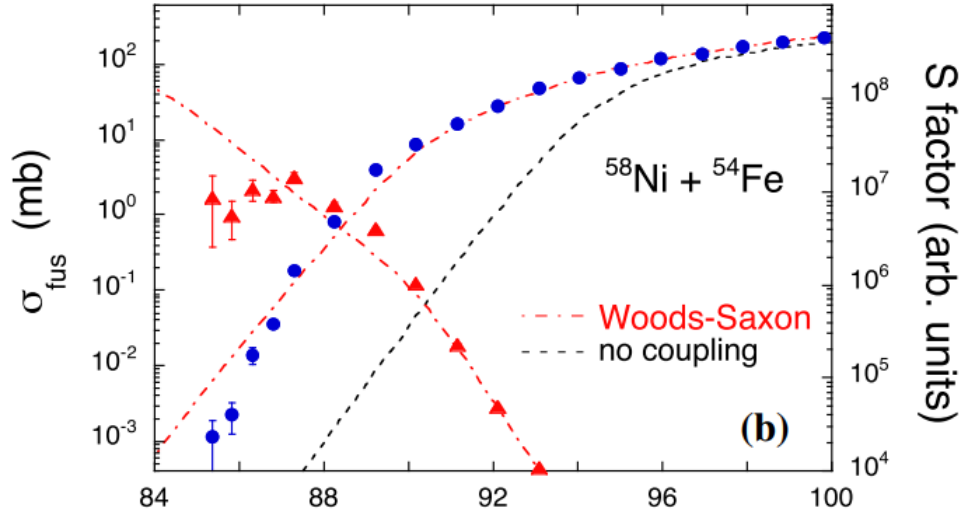The figure below shows another system ^{58}Ni+^{54}Fe with a negative Q-value (Q = -56.5 MeV).

Figure 1.12: Fusion excitation function of ^{58}Ni+^{54}Fe compared with a coupled-channels calculation and with the Wong's prediction (no-coupling), the red triangles represent the S-factor [40].

Also in this case there is a decrease steeper than the prediction of a coupled-channels calculation. At the same time, the figure shows an enhancement with respect to the one-dimensional model (no coupling). In the same figure, the S-factor is represented (red triangles). As expected there is a maximum and in correspondence of this energy, the cross section decrease starts. The analysis of systems with positive Q-values will be performed in the following lines.

1.3 Medium-light systems

These medium-light systems have a Q-value for the fusion which is positive. This has some implications, the astrophysical factor S(E) does not necessarily develop a maximum, so hindrance may not appear. Several experiments have shown that this S-factor maximum exists even if it is more broad [41] with respect to heavy systems. This maximum, which corresponds to the energy threshold (E_s) for hindrance, can be parametrized by the following formula [42]:

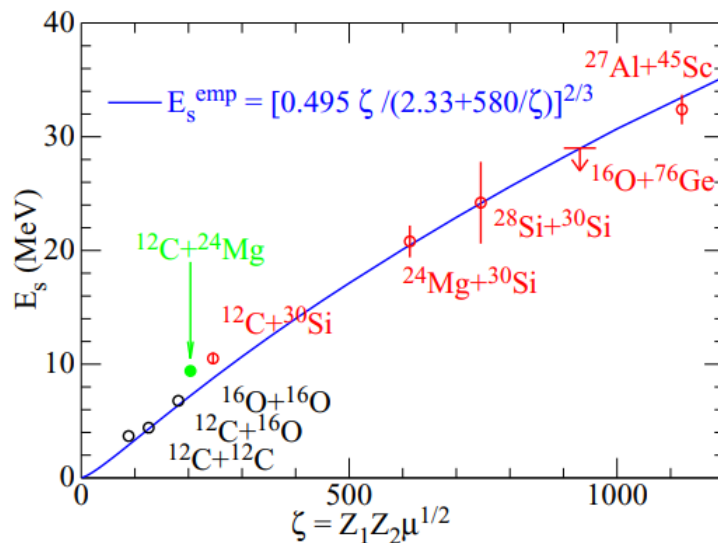$$E_s = \left(\frac{0.495\zeta}{(2.33 + 580/\zeta)} \right)^{2/3} \tag{1.40}$$

Figure 1.13: E_s in several systems. The red dots are the experimental values and the black open circles are obtained by extrapolation. [42].

Another critical aspect of these light systems is their crucial role in astrophysical scenarios [43]. Reactions like ^{12}C+^{12}C, ^{12}C+^{16}O or ^{16}O+^{16}O, have their effects in [36]:

- the evolution of the post-main sequence stars;

- the ignition of supernovae;

- accreting carbon-oxygen white dwarfs;

- the ignition of superbursts of neutron stars.

These reactions have been studied in several experiments, for example ^{16}O+^{16}O [44-45-46-47-48], ^{12}C+^{16}O [49] and ^{12}C+^{12}C [50-51-52-53-54]. The problem of these measurements is the presence of large uncertainties and of large discrepancies between the results of the different experiments, especially at the sub-barrier energies where the hindrance may occur. The presence of the hindrance would have a crucial role in the dynamics of stellar evolution [43]. A solution then is to study systems lightly heavier like ^{12}C+^{30}Si, ^{24}Mg+^{30}Si or ^{12}C+^{24}Mg. These reactions do not play a central role in astrophysical scenarios but their analysis can be useful in order to extrapolate the behavior of the interesting systems for astrophysics.

This is the reason that led to the choice of the reaction ^{12}C+^{30}Si that will be investigated in this thesis. Before going into more detail, let's first analyze briefly the results of the other two cases.

$^{24}Mg+^{30}Si$

An experiment on this system was performed a few years ago with the aim of observing the hindrance at low sub-barrier energies. This reaction has a positive Q-value = 17.89 MeV and a Coulomb barrier, in the center of mass frame, of 24.7 MeV. In the figure below one can see how a coupled channels calculation using a Wood-Saxon potential fits well the data above the Coulomb barrier but overpredicts the fusion cross-section for energies below the barrier. This is a clue of the presence of hindrance [55].
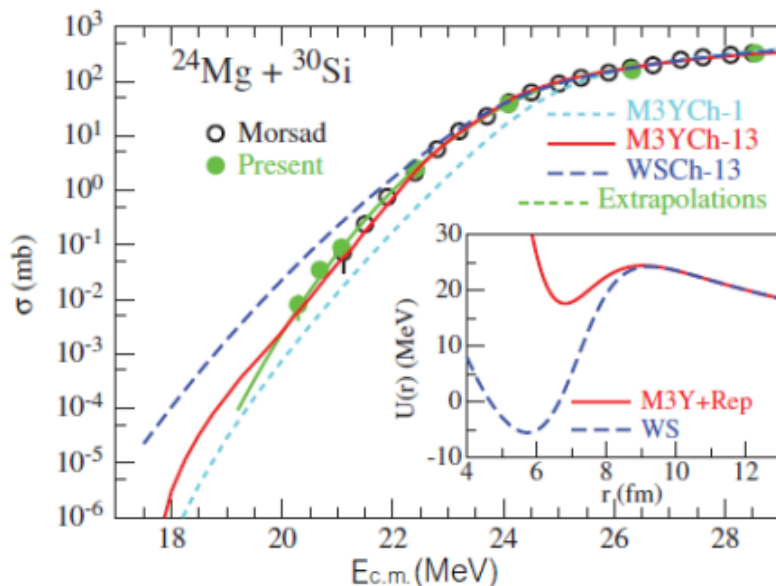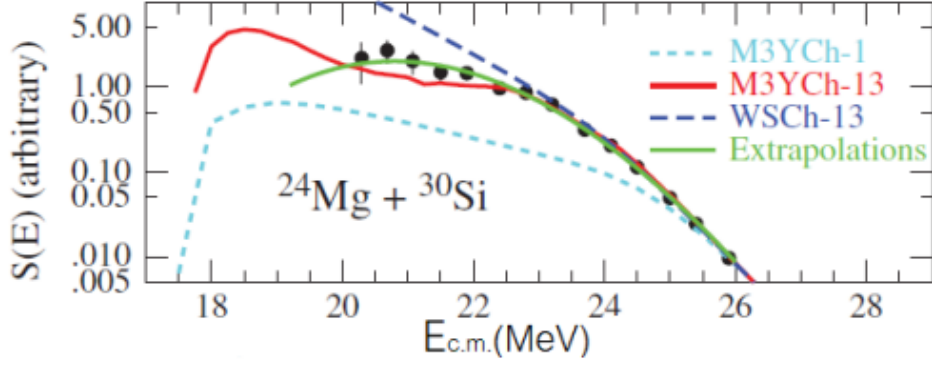

Figure 1.14: Experimental excitation function for ^{24}Mg+^{30}Si compared with several coupled channels calculations [55].

As explained previously, a more convenient way to see the hindrance is by plotting the astrophysical S-factor S(E).

Figure 1.15: S(E) for ^{24}Mg+^{30}Si [55].

In Fig. 1.15 there is the second evidence for the presence of hindrance: S(E) displays a maximum at energy around 20.8 MeV, in the same range starts the deviation between the coupled-channels calculation and the experimental measurements. The threshold value for hindrance is also in agreement with the parametrization in Eq. 1.40.

$^{12}C+^{24}Mg$

Several measurements of the excitation function for ^{12}C+^{24}Mg were performed, one of which at LNL [56]. As in the previous case, the Q-value is positive (16.3 MeV) while the Coulomb barrier is around 11.5 MeV.
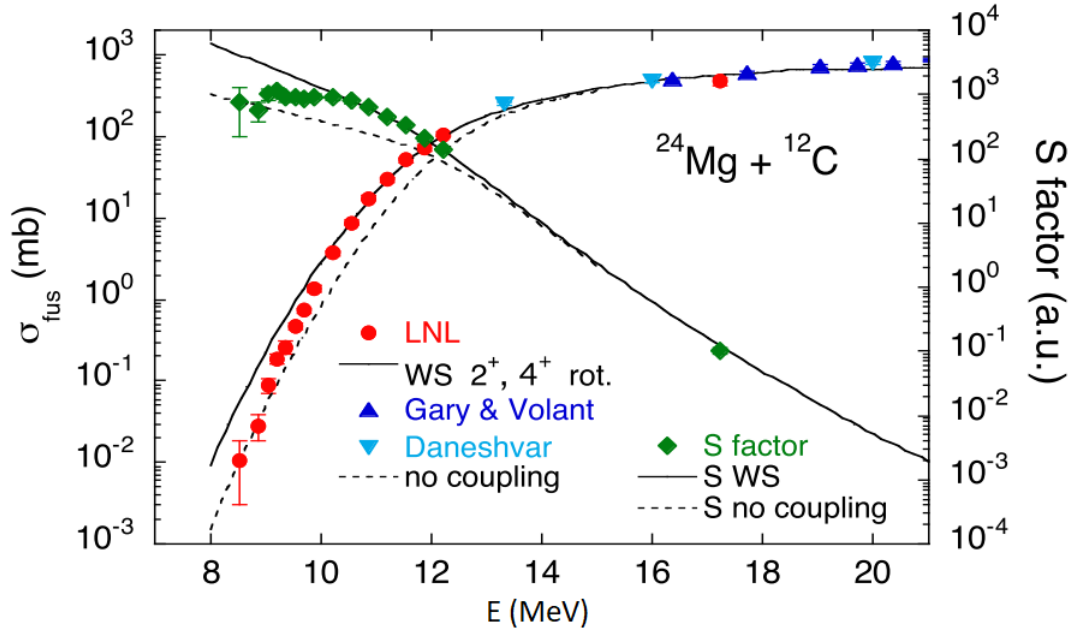
Figure 1.16: Fusion excitation function for ^{12}C+^{24}Mg, in red dots there are the results of the experiment performed at LNL. In green there are the S-factor values [36].

From Fig. 1.16 it is clear the presence of the hindrance. First of all, the coupled channels calculations overpredict the fusion cross-section for sub-barrier energies. Then, the S-factor has a maximum of around 10.2 MeV, which can be taken as the threshold for hindrance. This value is in agreement with the parametrization proposed by C.L.Jiang et al. in Eq. 1.40.

Chapter 2

The experiment

2.1   Description

The heavy-ion fusion reaction ^{30}Si+^{12}C has been studied during a test experiment performed in July 2022 at Laboratori Nazionali di Legnaro. The experimental setup consists of the XTU Tandem accelerator and two detectors: AGATA and EUCLIDES.
Tandem accelerator delivered a ^{30}Si beam at two different energies on a ^{12}C target. The collision takes place inside a scattering chamber where the vacuum is realized. Inside the scattering chamber the EUCLIDES array of silicon detectors is placed at 6.2 cm from the target, while outside the chamber, the spectrometer AGATA is devoted to the gamma detection.
The experiment has the goal of measuring the fusion cross-section. In the past, many experiments were based on the detection of the evaporation residues or on the γ-rays emitted by the compound nucleus. The problem with these techniques is the presence of a lot of background overlying fusion events at sub-barrier energies. In light of this, a new approach is necessary. In this test experiment the attempt is to obtain a value for the fusion cross-section using a combined set-up of AGATA and EUCLIDES. The idea is to use the coincidences technique: the Si detector array EUCLIDES is used for detecting the light-charged particles evaporated by the compound nucleus while the γ-ray spectrometer AGATA is used to measure the photons emitted by the evaporation residues. The innovation of this technique, with respect to other past fusion experiments, consists in the fact that by comparing the time stamps of the two events we consider only the coinciding events, i.e. relating to the same fusion event. In this way, a lot of background events is excluded.

$\underline{^{30}Si+^{12}C \ with \ Pisolo}$
Before starting to describe in detail the experimental setup, it is worth reviewing the results of a previous experiment on the same reaction performed at Laboratori Nazionali di Legnaro [1].
Also in that case the experiment was performed in inverse kinematics with the ^{30}Si beam delivered by Tandem accelerator with a current around 10 pnA. The ^{12}C target has a thickness of 50 µg/ cm^2 enriched to 99.9% in mass 12. The experimental setup is composed of different components: a reaction chamber, an electrostatic deflector, two microchannel plates and an ionization chamber that contains a silicon detector.
In the reaction chamber there are 4 silicon detectors placed at 16° that are used to normalize the fusion yields to the Rutherford scattering cross-section. The electrostatic deflector at forward angles is used to suppress the transmitted beam events and to separate them from the evaporation residues. The separation is made by exploiting the different electrical rigidity. The two microchannel plates measure the time of flight and, combining it with the ΔE-E information obtained by the ionization chamber and the silicon detector, it is thus possible to distinguish the beam events which, despite the suppression, arrive on the detector telescope and the fusion events.
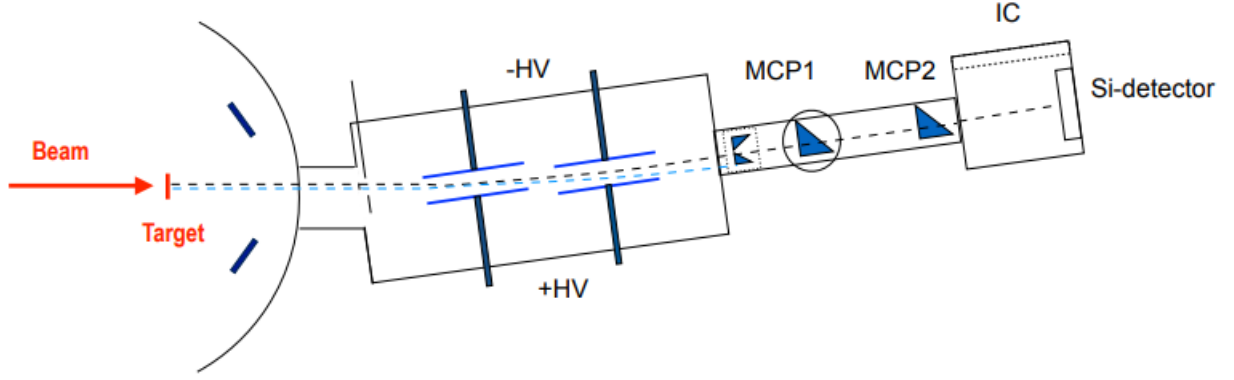
Figure 2.1: Experimental setup with the different components: the reaction chamber, the electrostatic deflector, the two microchannel plates and the ionization chamber [57].

The fusion cross-section is obtained by detecting the evaporation residues and measuring the angular distributions in the range $-6 < \theta < 10$ at three different energies in the laboratory frame $E_{lab} = 45, 59, 80$ MeV and then they are angle integrated in order to derive total fusion cross section. The experimental excitation function compared with different coupled channels calculations are represented in the next figures.
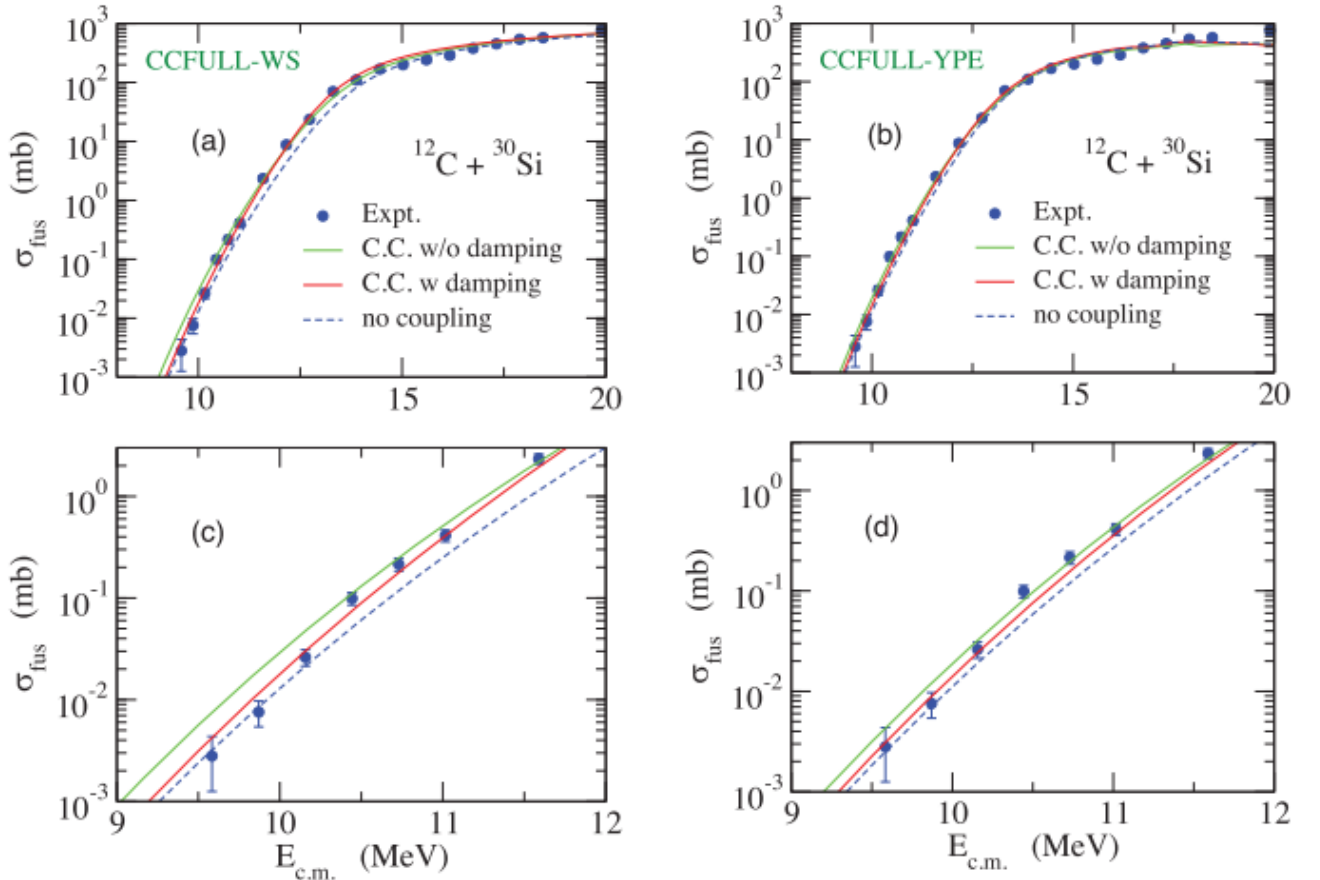

Figure 2.2: Experimental excitation function compared with coupled channels calculations using a Wood-Saxon(WS) potential and a Yukawa-plus-exponential(YPE) potential. Both calculations were considered with and without damping of coupling strengths. Figures c) and d) show a zoom in the region 9-12 MeV energy in the center of mass frame [1].

The coupled channels calculations were performed considering a Wood-Saxon potential with the following values for its parameters [1]:

V_0 [MeV]	r_0 [fm]	a_0 [fm]
48.24	1.1	0.61

Table 2.1: Parameters for the Wood-Saxon potential.

Regarding the nuclei the ^{12}C is considered inert while the ^{30}Si vibrational and also were taken into account the coupling with two states. The detailed pieces of information are reported in the next table [1]:

J^P	E [MeV]	β_J
2^+	2.235	0.33
3^-	5.487	0.275

Table 2.2: ^{30}Si states considered in the coupled channels calculations.

Looking at Fig. 2.2, can be observed how the experimental fusion cross-section starts to drop down compared to the coupled-channels calculation. This drop at the sub-barrier energies can be taken as the first evidence of the fusion hindrance phenomenon.

Other possible checks in order to confirm the hindrance are by looking at the logarithmic slope L(E) and at the astrophysical S-factor.
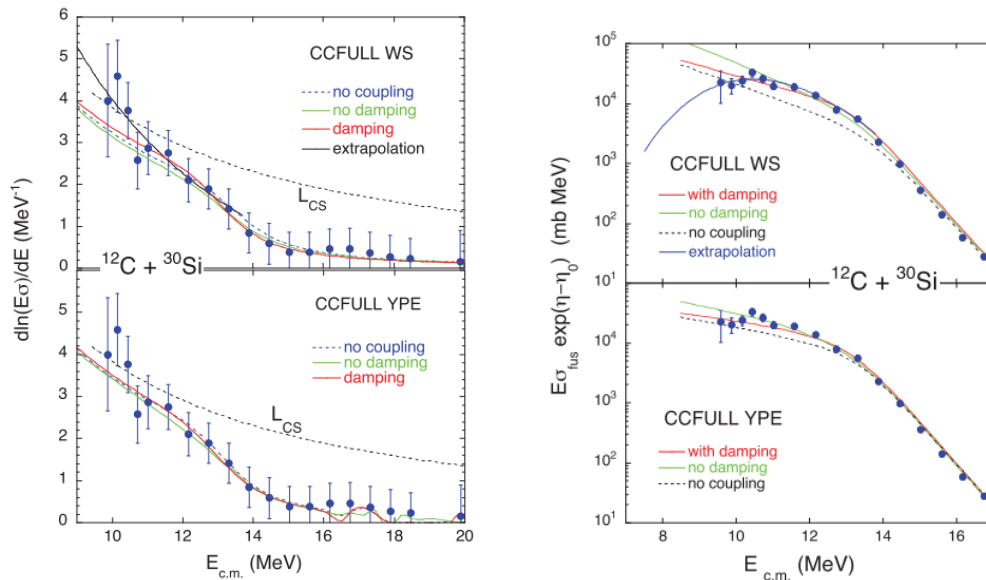

Figure 2.3: In the left panel the experimental logarithmic derivative compared with the coupled-channels calculations, in the right panel the comparison between the experimental astrophysical S-factor and the coupled channels calculations [1].

Fig. 2.3 confirms the presence of the hindrance: the S-factor develops a maximum around an energy of 10.5 MeV, even if the calculations do not reproduce the data. At the energy where S(E) has a maximum, if hindrance occurs, the L(E) and L_{CS}(E) must cross at this energy.

2.2   Accelerator system

The ^{30}Si beam is generated by an external ion source with a positive charge-state (q = +1), then interacts with the Cesium (in a gaseous state), and its charge state changes to q = -1.

It consists of a tank that contains 7 atm of SF$_6$ (Sulphur hexafluoride), an insulating gas that is used to prevent sparks towards the tank and along the accelerating column. Inside the tank, there is a high-voltage terminal at its center. At this stage, the negative ions are accelerated from the ground voltage to the terminal voltage which can reach a value of 14.5 MV. The terminal is charged by two laddertrons. The high-voltage terminal contains a carbon foil with a thickness of 5 µg/cm^2. The foil strips some electrons off the beam changing the charge state. In this experiment the ^{30}Si had a charge state of 6 (q = +6). The ions are positively charged and so undergo a second acceleration until the end of the tank where the beam is focused by several magnets against the target.
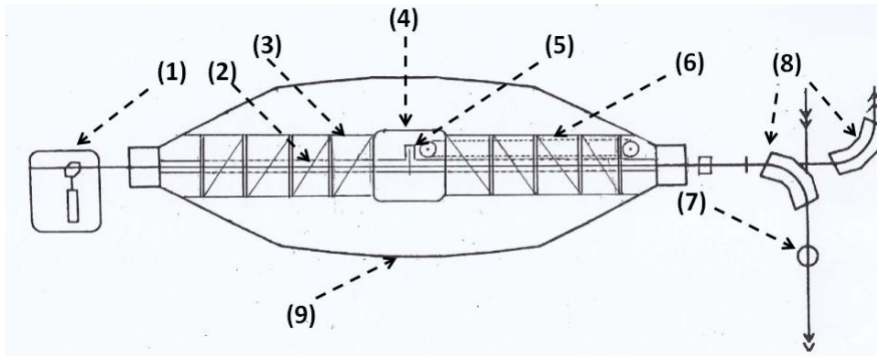

Figure 2.4: Tandem schematic view: the ion source(1), the accelerating tube(2), the column(3) which supports the high- voltage terminal(4), the stripper foil(5), the laddertrons(6), the beam diagnostics station(7), bending magnets (8), the tank filled with SF$_6$(9) [58].

The natural ^{12}C target has a 0.1 mg/cm^2 thickness. It contains some impurities, mainly deuterium which produces an unwanted background in the EUCLIDES events.

2.3   AGATA

AGATA (**A**dvanced **GA**mma **T**racking **A**rray) is a European project based on the tracking of the γ-rays.

The γ-ray spectroscopy plays a central role in Nuclear Physics studies because these γ-rays are emitted during the de-excitation of a nucleus during a transition between two states. Measuring them allows the obtaining of several important information on the states. In order to understand how AGATA works it is necessary to start with the matter-radiation interaction mechanism. The ways in which radiation interacts with matter are mainly 3: the photoelectric effect, the Compton scattering and the pair production.

Photoelectric effect

In this effect the incoming photon, with an energy E$_\gamma$ = hν, interacts with an atom of the medium. The result is the emission, from one of the atomic orbitals, of a photoelectron with an energy E$'_\gamma$:

$$E'_{\gamma} = E_{\gamma} - B_e$$

where B$_e$ is the electron binding energy of the orbital. This kind of interaction is predominant for photons of low energy, in the range of hundreds of keV. The cross-section depends on both the energy of the photon and the atomic number Z of the medium :

$$\sigma_{ph} \propto \frac{Z^4}{E_{\gamma}^3}$$

Compton scattering
A photon with an energy E_γ scatters with an electron of the medium. The scattered photon has a lower energy E'_γ that depends by the scattering angle θ:

$$E'_\gamma = \frac{E_\gamma}{1 + \dfrac{E_\gamma}{m_e c^2}(1 - cos\theta)}$$

This kind of interaction dominates in an intermediate range between 1-10 MeV. The cross-section increases linearly with the Z of the medium. The angular distribution for the scattered photons is given by the Klein-Nishina formula [59]:

$$\frac{d\sigma}{d\Omega} = Z\,r_e^2 \left(\frac{1}{1 + \alpha(1 - cos\theta)}\right)^2 \left(\frac{1 + cos^2\theta}{2}\right)\left(1 + \frac{[\alpha(1 - cos\theta)]^2}{(1 + cos^2\theta)[1 + \alpha(1 - cos\theta)]}\right)$$

where r_e is the classical electron radius and $\alpha = h\nu/m_e c^2$.

Pair production
This process is present only under the condition $E_\gamma > 2m_e c^2$. The photon can produce an electron-positron pair, after the positron annihilation two photons of 511 keV are emitted. Pair-production is the dominant process for photon energies of the order of 10 MeV. The cross-section has the following dependency on the atomic number of the medium:

$$\sigma_{pp} \propto \sqrt{Z}$$
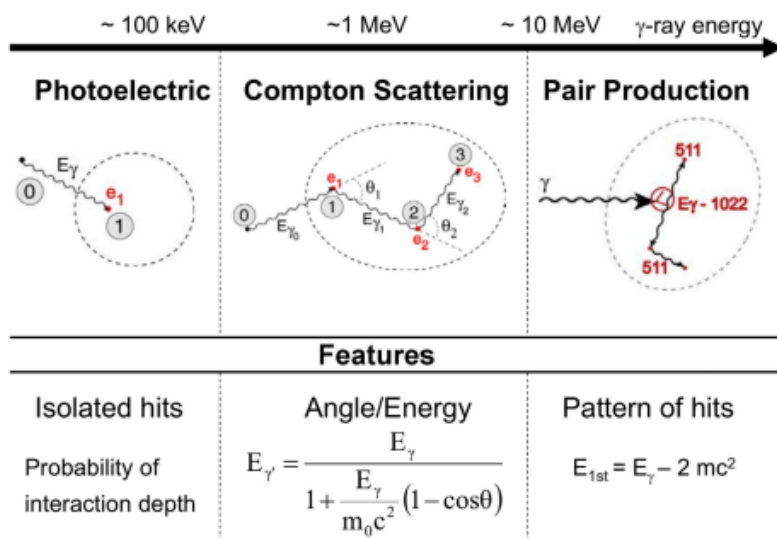
A summary table is shown below:

Figure 2.5: Radiation-matter interaction mechanism schematized according to their relevant energies and the the features used by the tracking algorithms in AGATA [60].

The main mechanism in Nuclear Physics spectroscopy studies is the Compton scattering. In this process may happen that the radiation does not release all its energy inside the detector which brings to the increase of the background. A first solution of this inconvenient was to surround the γ detectors with some other detectors that work as a veto, i.e. they suppress the Compton events where all not the entire energy was deposited inside the detection volume. These veto detectors, also called anti-Compton shields, consisted of bismuth germanate (BGO) scintillator crystals. This addition brings an increase in the peak-to-total (P/T) ratio. But, on the other hand, this new setup had its drawbacks. The presence of the anti-Compton shields limited the solid angle covered by the γ detectors and consequently, the efficiency got worse.

In order to overcome this problem the AGATA γ-ray tracking spectrometer has been thought. This project is still ongoing. When it will be complete, AGATA will consist of 180 HPGe electrically segmented crystals that would cover the entire 4π solid angle. The use of electrically segmented crystals allows the localization of the interaction points of the γ-rays inside the germanium crystals volume with a precision up to 5 mm. At the same time, the deposited energy can be determined with high resolution. Knowing the coordinates of every interaction via PSA (Pulse-Shape-Analysis) and combining it with 'tracking' algorithms, it is possible to reconstruct the trajectories of the γ-rays. Further details on the Pulse-Shape-Analysis and on tracking algorithms will be given in this chapter. The knowledge of the direction of the emission for the γ-rays is fundamental for a precise Doppler correction.

The choice of the Germanium for the crystals was dictated by several reasons:

- a low energy band gap ($\sim$ 4 eV at 300 K). This low value does not allow the functionality of the HPGe detector at room temperature because the thermal excitation will permit electrons to overcome the band gap and create the leakage current. The problem is solved by using liquid nitrogen at a temperature between 70-90 K to cool the detectors ;

- a low mean energy necessary to create an electron-hole pair ($\sim$ 3 eV/pair). This implies a very good resolution, better than the scintillator ones;

- relatively high atomic number (Z = 32) that increases the cross-section for photoelectric effect.

These HPGe crystals are divided into 60 triple cluster (ATC), each one composed of three asymmetric crystals. The crystals' dimensions are 90 mm in length and 80 mm in diameter. Every crystal is encapsulated into a sealed aluminum canister. Each crystal is electrically segmented into 36 parts, six along the azimuthal direction and six along the longitudinal one. Every segment of each crystal is labeled. Along the longitudinal direction the labeling is made with a number from 1 to 6, and the azimuthal segmentation is labeled with a letter from A to F. Each crystal gives 38 signals: the 36 corresponding to each segment plus 2 for the core.
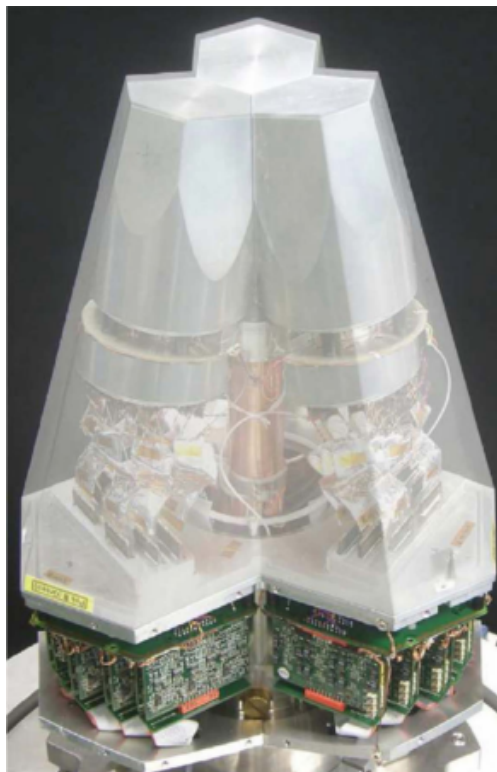

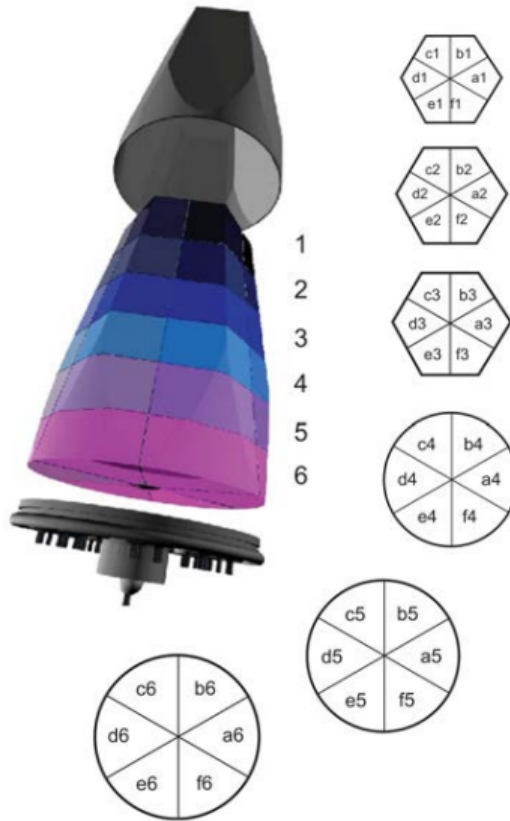Figure 2.6: Three HPGe crystals with their electronics [61].

Figure 2.7: Scheme of the labelling for a AGATA crystal [62].

For the experiment treated in this thesis, 11 ATC have been used for a total of 33 crystals of which, however, 3 were not considered in the analysis because they were noisy [63].
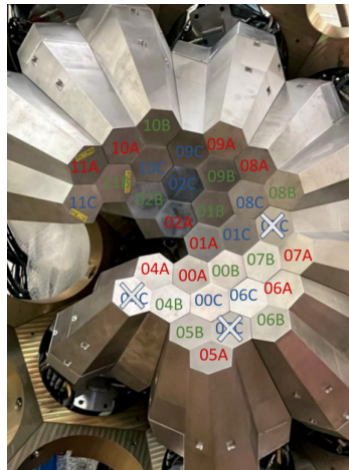

Figure 2.8: Crystals used for the experiment described in the thesis. Crystals 04C, 05C and 07C are crossed out with an x because they were not included in the analysis [63].

As mentioned in the previous lines, this tracking spectrometer is based on the determination of the energy, time and position of every interaction point of the γ-rays via PSA and subsequently the reconstruction of the γ-rays trajectories through a tracking algorithm.

The peculiarity of a segmented detector is that charges are induced also in the neighboring electrodes and not only in the segment where the γ-ray has interacted creating electron-hole pairs. The induced signals are called transient signals whereas the signal generated in the segment where the interaction occurred is called net-charge signal. The Pulse-Shape-Analysis (PSA) algorithm compares these signals

with a library of traces obtained via simulation. Fitting the net charge signals and transient signals it is possible to obtain the interaction point with a precision of few millimeters [64]. The comparison between the measured and the simulated signals is performed by minimizing the figure of merit (FOM) [65]:

$$FOM = \sum_{j_i, t_i} = |A_{j,m}(t_i) - A_{j,s}(t_i)|^p$$

where $A_{j,m}$ is the measured signal in the segment j at time t_i whereas $A_{j,s}$ is the simulated signal in the segment j at time t_i. p is a positive number.

The energy measurement is obtained by integrating the signal. Thanks to the tracking algorithm and using the position information of every interaction point one can reconstruct the trajectory of the photon whereas with the energy information, it is possible to obtain the full photon energy.

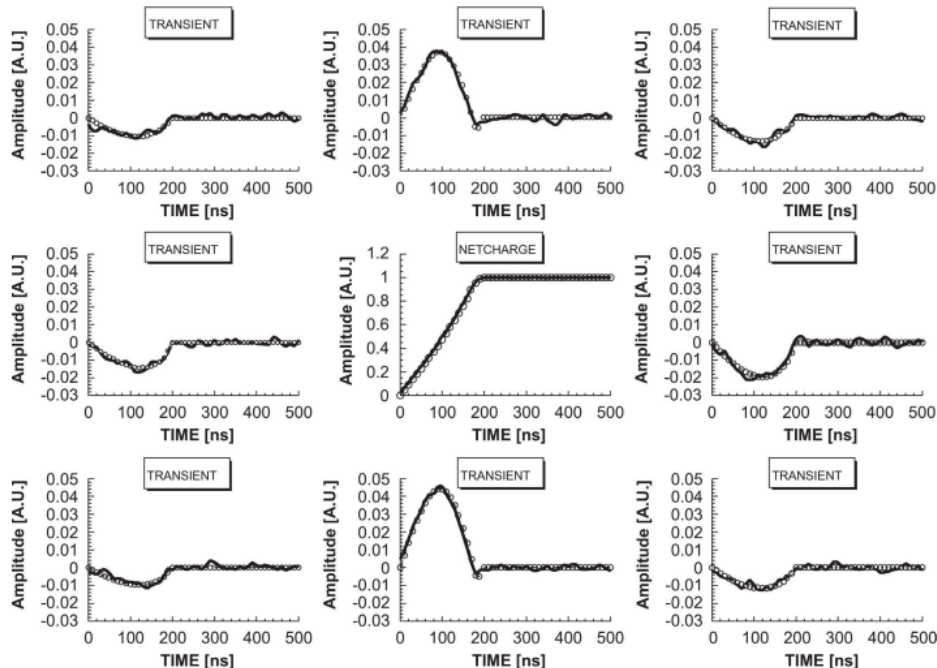An example of a PSA analysis is shown in the next figure.

Figure 2.9: Comparison between a measured signal (solid line) and a simulated one (circles). 9 signals are shown: a net charge signal and 8 transient signals [66].

2.4 EUCLIDES

EUCLIDES (**EU**roball **C**harged **L**ight particle **I**dentification **DE**tector **S**phere) is a Si detector array that is used to detect the light-charged particles (α, p) emitted by the compound nucleus. This detector has already been employed in several experiments, one of which at Legnaro [67].

The device consists of 40 two-stage ΔE-E telescopes positioned in a polyhedron composed of 42 faces: 30 with an irregular shape and 12 with a pentagonal shape. Two of these pentagonal shape faces are open and are used in the following way: one allows the passage of the incoming beam, and the other permits the passage of the residual ^{12}C beam that has not interacted and of the evaporation residues. Regarding the hexagonal telescopes, in the forward region, 5 of them are segmented into 4 equal parts. The ΔE and E stages have a thickness of about 130 µm and 1000 µm respectively. Their capacitance values are 850 pF for the ΔE stage and 130 pF for the E stage while the resistivity values are 3 kΩ/cm and 18 kΩ/cm respectively. The geometrical area covered by the two detectors is the same and is around 10.2 cm^2. They are separated by a kapton spacer 100 µm long. The nearby telescopes are connected together with Al bridges in such a way that the distance between nearby telescopes is $\sim$ 0.2 mm. The solid angle coverage is $\sim$ 81% for the ΔE and $\sim$ 80% for the E.

The details for the different face shapes are reported in the next table [67]:

shape	pentagonal	hexagonal	hexagonal segmented	full
Segmented parts	1	1	4	1
Solid angle coverage	$\sim 2.1\%$	$\sim 2\%$	$\sim 2\%$	$\sim 81\%$
#	10	25	5	40

Table 2.3: Composition of the Si array with the information on the segmented parts, solid angle coverage and number of detectors according to their shapes.

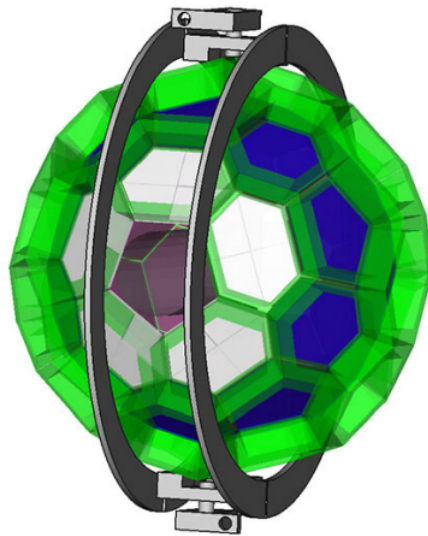A colored schematic view of the detector can be seen in the figure below.

Figure 2.10: View of Euclides: in gray the two specular open faces that allow the passage of the beam. In white the 5 segmented hexagonal telescopes [67].

As mentioned in the previous lines, EUCLIDES is inserted in a reaction chamber where in the center there is the ^{12}C target.
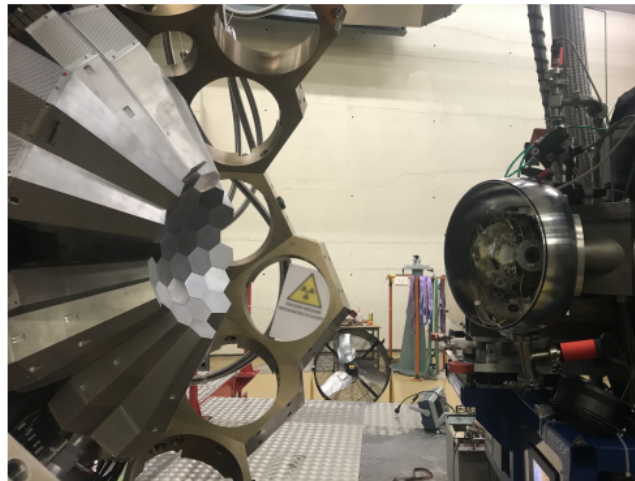

Figure 2.11: Experimental setup: on the right the reaction chamber with Euclides, inside it there is the target. On the left the γ-spectrometer AGATA [68].

The physical principle according to which EUCLIDES works is the following: charged particles penetrating or traversing the detector create electron-hole pairs. The electron-hole pairs are separated by an electric field and drift to the electrodes. The signal collected by the electrodes is proportional to the energy released by the light-charged particle. Like most semiconductor detectors, EUCLIDES has a pn junction where the p-side is a single area whereas the n-side, doped via a high energy implantation, is segmented into 4 channels. The anodes of the telescopes are put at ground whereas the cathodes are biased positively.

By collecting the ΔE information in the first stage and the E information in the second it is possible to understand the light charged-particle that crosses the detector. The detection is based on the Bethe-Bloch equation in the non-relativistic approximation:

$$\Delta E \propto \frac{Z^2 A}{E} \tag{2.1}$$

where Z and A are the atomic number and the mass number of the incident particle respectively. So looking at a ΔE-E plot there is the possibility to discriminate between the different light charged-particles, more information will be given in the next chapter.

Chapter 3

Data analysis and results

In this chapter the data analysis and the obtained results will be explained in detail. Before addressing these themes, a brief description of the experimental procedure is necessary.

As mentioned in the previous chapter, this test-experiment was performed in July 2022 for three days. The Tandem accelerator provided the ^{30}Si beam at two different energies: 47 MeV, above the Coulomb barrier, and 40 MeV, below the Coulomb barrier. Before starting the acquisition it was necessary to focus the beam. This procedure was performed by putting a quartz crystal in the reaction chamber in the position of the target. Then the beam was delivered and focused to the quartz center. First, this was done for the beam energy of 47 MeV. After the check of the beam quality, the crystal was replaced by the target and the surrounding EUCLIDES detector. Then, several runs at this energy were measured. Before starting the acquisition at 40 MeV all this procedure had to be repeated.

In this thesis 5 different runs have been analyzed, they were labeled as follows:

Run	Energy
1	47
2	47
3	47
4	40
5	40

Table 3.1: Run analyzed

During the analysis, another run was studied, however, it created problems because during its acquisition there were some malfunctions in AGATA electronics. Then the run was stopped and restarted a couple of times. Due to these problems this run has not been analyzed.

3.1 Gamma-ray spectra

The study of the spectra of AGATA is important for several reasons: it allows the study of the coincidence events where the compound nucleus has evaporated only neutrons. This is because the neutrons, being chargeless particles, do not leave any signal in EUCLIDES. Another reason for the study of AGATA spectra is the calculation of EUCLIDES efficiency.

In the study of a gamma-ray spectrum, it is important to take into account the Doppler effect, i.e., the γ-ray is emitted at a characteristic energy E_0 in the evaporation residue rest frame, but in the laboratory frame it undergoes a shift in energy. This shift depends on the velocity of the evaporation residue and the angle θ of the γ detection with respect to its moving direction.

The relation between the photon energy in the laboratory frame (E_{lab}) and its characteristic value

(E_0) is the following:

$$E_{lab} = E_0 \, \frac{\sqrt{1 - \beta^2}}{1 - \beta \cos\theta} \tag{3.1}$$

The Doppler correction was performed by using an average β value of 4% and the angle θ obtained by combining the PSA and the tracking information of AGATA. A comparison between the Doppler corrected spectrum and the one non-corrected is reported in the figure below.
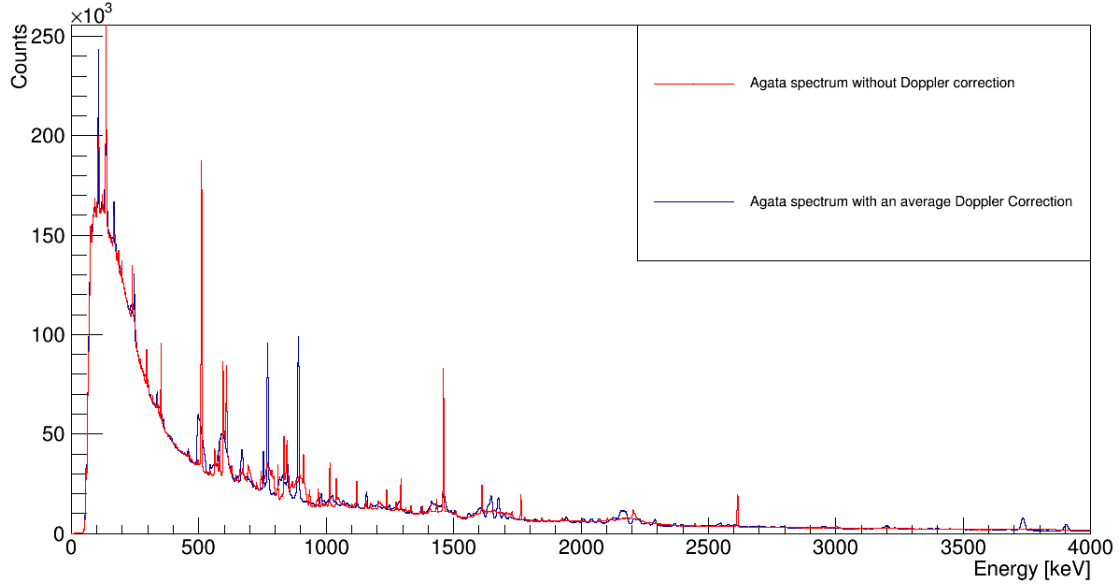

Figure 3.1: In red the γ spectrum for a 47 MeV run without Doppler correction, in blue the spectrum with the Doppler correction.

3.2 EUCLIDES spectra

As explained in the previous chapter, EUCLIDES is an array of Silicon detectors that provides information on the energy released (ΔE) in one stage and the residual energy measured in a second stage. Exploiting the Eq. 2.1 and plotting the data in a E-ΔE graph it is possible to discriminate between the different light-charged particles evaporated by the compound nucleus.
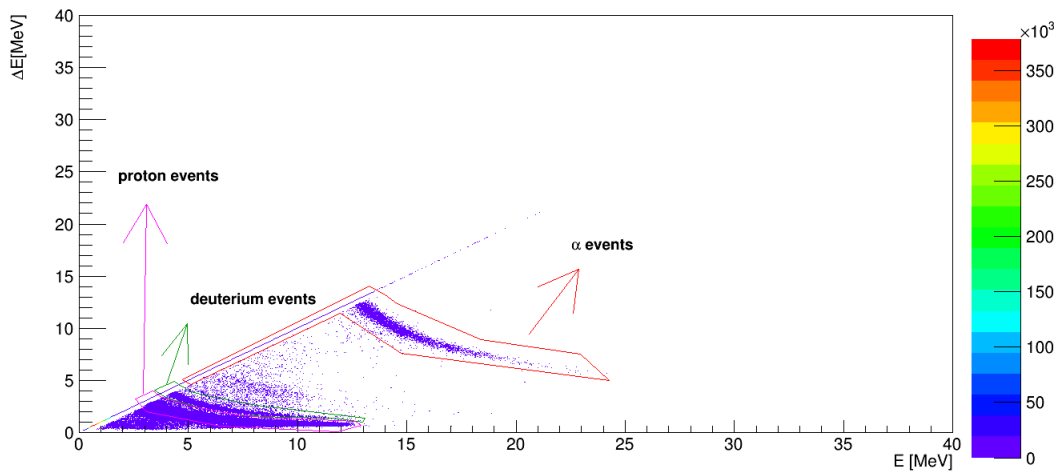

Figure 3.2: Euclides ΔE-E spectra where three different regions are well visible.

Fig. 3.2 displays an Euclides spectrum for one of its telescopes. Three hyperbola-shaped structures

can be observed, each one corresponding to a different light-charged particle evaporated: protons, deuterium or alpha. The next step consists in performing some cuts in these three regions. In this way one selects the events of interest and, using the software Selector, can obtain a coincidence spectrum with Agata. Looking at the spectrum the diagonal was included in the cuts. This is because some particles, due to their low energy or their high mass like α- particles, are completely stopped in the first stage ΔE without leaving any signal in the second stage. This means that their total energy is equal to the energy released in the first stage → E = ΔE and then the event lies on the diagonal. However, not in all spectra of the 40 telescopes the three hyperbola-shaped structures are present. This is due to kinematics reasons: both protons and alphas are emitted with substantially lower energy at backward angles, so that at those angles α particles will not be detected at all. This is confirmed by the figure below.

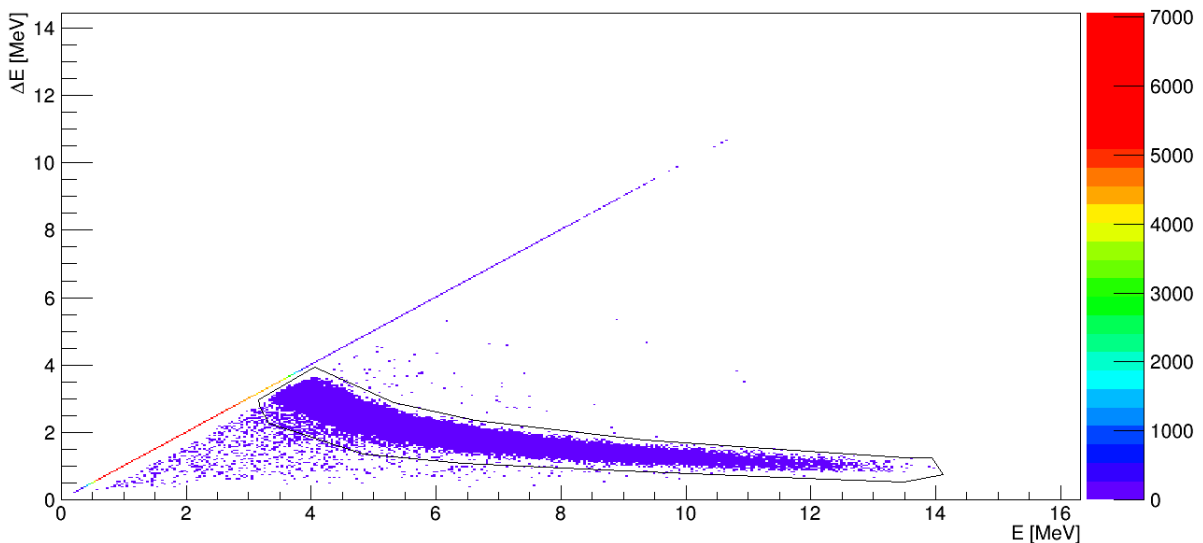Figure 3.3: Euclides ΔE-E spectra for a telescope placed at $\theta \sim 122°$. In this case only protons were detected.

3.3   Coincidences gamma-particles

Now it is possible to merge the Agata spectrum with the Euclides' cuts in order to obtain the coincidences gamma-particles, whose study allows to count the fusion events. The data are selected according to the difference in the timestamps of Agata and Euclides. Each event of the two detectors has its time (called timestamp), so that the difference between the Euclides and the Agata timestamps yields a timestamp spectrum. The coincidence spectrum is obtained by selecting a window of timestamps difference. The window is chosen so as to contain the coincidence peak where the events show a correlation between a light-charged particle and the γ ray. The window has also to be chosen as narrow as possible in order to get rid of uncorrelated events and reduce the background.
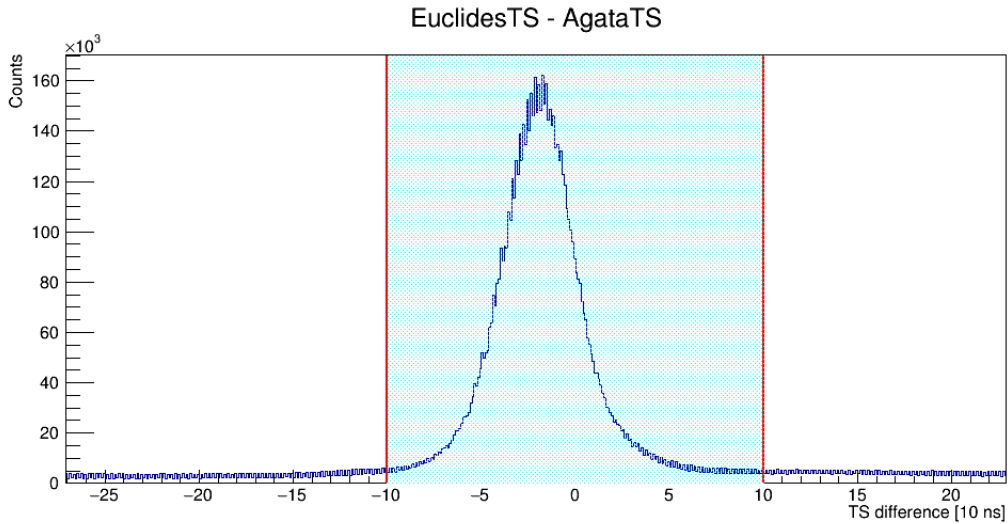
Figure 3.4: Spectrum of the timestamp difference between the EUCLIDES and AGATA events for run 3. The blue area represents the time coincidence window applied. The coincidence window has a width of 200 ns.

However, due to electronics problems, not in all the runs the coincidence window could be chosen so narrow.
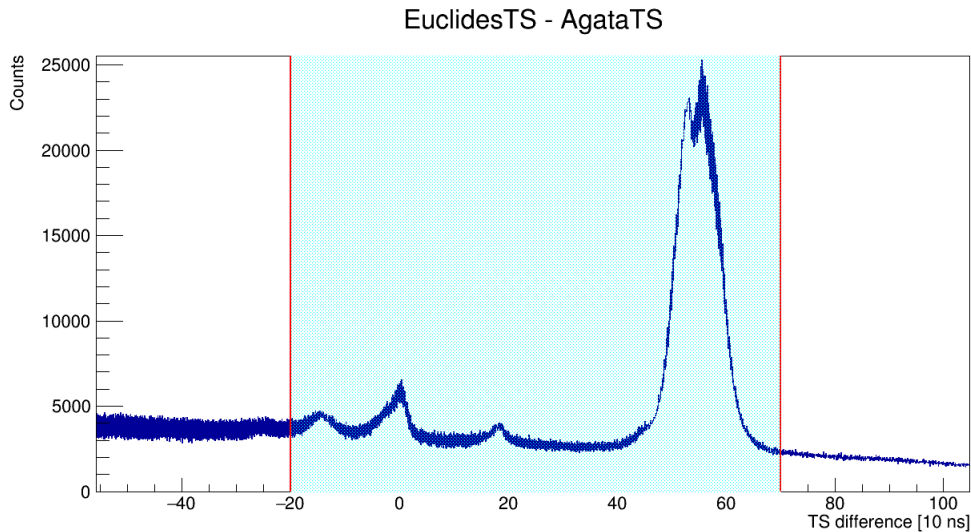

Figure 3.5: Spectrum of the difference of timestamp between the EUCLIDES and AGATA events for run 2. The coincidence window has a dimension of 900 ns.

In Fig. 3.5 the coincidence window was chosen more broadly in order to have more statistics. The drawback is the increase in the background.

After the selection of the coincidence time window, one obtains the coincidence spectrum. Also in this case the Doppler correction has to be performed. Two different methods were used: one using an average β and the other event per event.

In the average correction, an average value for β was considered and the angle θ was obtained via PSA and the tracking algorithm of AGATA. In the event per event correction, the value of the β of the evaporation residue was calculated for each single event. The value is obtained considering the momentum and energy conservation by exploiting the energy information measured by EUCLIDES. The angle θ was obtained by combining the PSA information and the angle of the EUCLIDES telescope. In the figure below a comparison is done between γ spectra in coincidence with particles, using these two Doppler corrections.
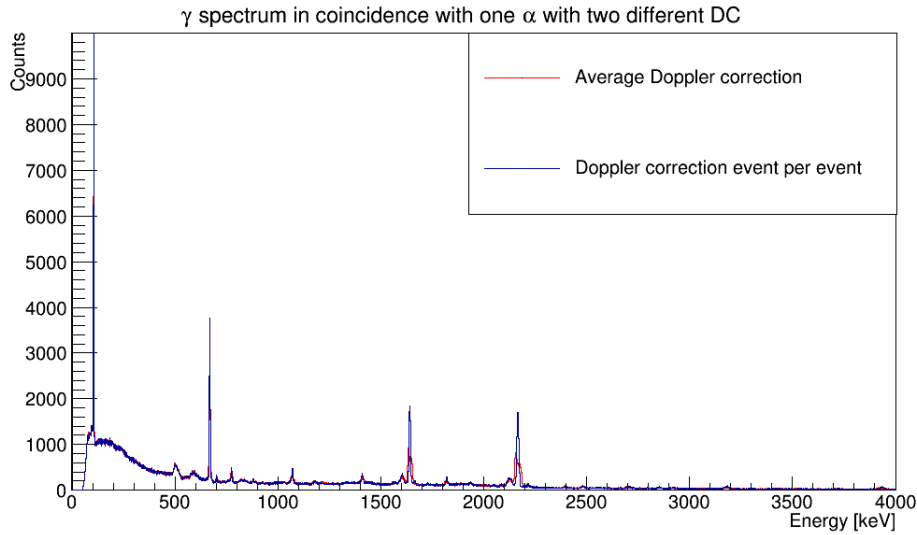
Figure 3.6: Comparison between the two spectra using two different Doppler corrections: in red is the average correction, in blue is an event per event correction.

In the analysis the spectra with the correction event per event were considered because this correction is more accurate.

3.4 Results

After having performed the coincidences between the AGATA and the EUCLIDES spectra it is possible to obtain the fusion cross-section σ_{fus} by measuring the number of fusion events N_{fus}. The relation between these two quantities is the next one:

$$\sigma_{fus} = \frac{N_{fus} A_t}{\varepsilon_{AG} * \varepsilon_{EU} * 3.76 * 10^6 * I(pnA) * \Delta t * t(mg/cm^2)} \tag{3.2}$$

where:

- N_{fus} is the number of fusion events;

- A_t is the atomic mass number of the target;

- ε_{AG} is the efficiency of AGATA;

- ε_{EU} is the efficiency of EUCLIDES;

- $I(pnA)$ is the beam current measured in pnA (particle-nano-ampere);

- $\Delta t(s)$ is the run duration in seconds;

- $t(mg/cm^2)$ is the target thickness.

In the next lines a description for each quantity contained in Eq. 3.2 will be given.

Number of fusion events N_{fus}

The number of fusion events is obtained by integrating the peaks related to gamma transitions of the evaporation residues that feed the ground state. The integration is done by performing a Gaussian fit with a linear background. If two peaks are close the integration is performed by using the sum of the gaussians. An example for each of these two cases is shown below.
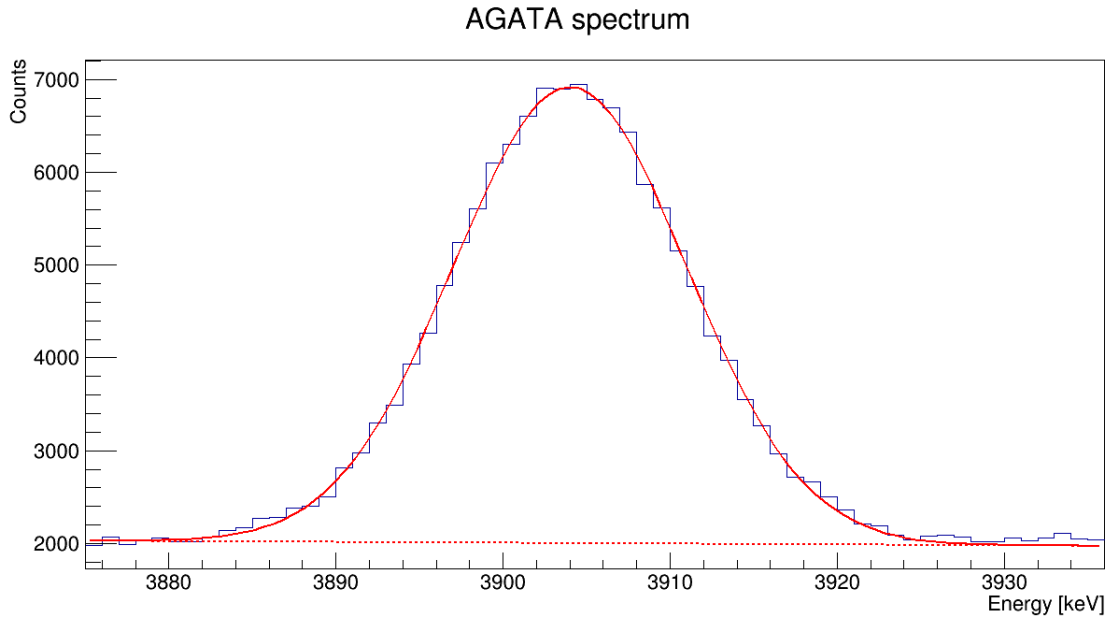
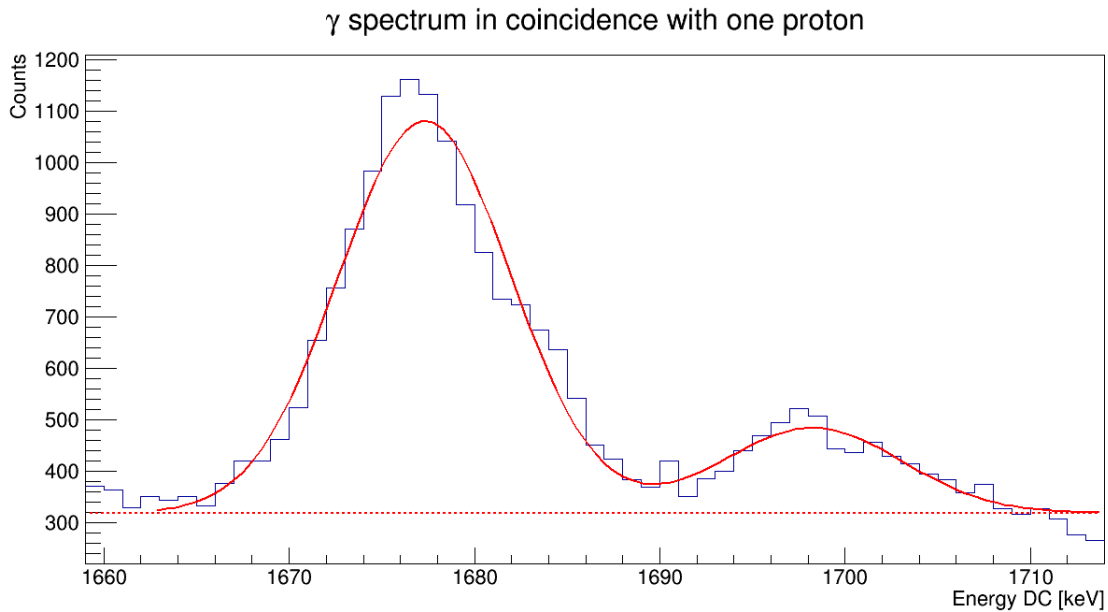Figure 3.7: Gaussian fit with a linear background for the 3904.4 keV peak of ^{40}Ca .

Figure 3.8: Fit using two gaussians with a linear background for the 1677.2-16998.0 keV peaks of ^{41}K .

The number of fusion events is the sum of two contributions: the events where only neutron evaporation takes place and those where there is the emission of at least one charged particle.

The first kind of events is obtained by integrating only the Agata spectrum with the Doppler correction and without the coincidence with EUCLIDES (see Fig. 3.1). The second kind of events is given by integrating the peaks present in the coincident spectra AGATA-EUCLIDES. Another approach was to study the excitation energy as a function of the gamma energy and project this 2D-histogram on the gamma-ray energy axis (further details will be given in the next lines).

<u>Neutron transitions</u>

These transitions are studied by analyzing the spectra of only AGATA. The AGATA-spectrum for run 3 is displayed in the next figure.
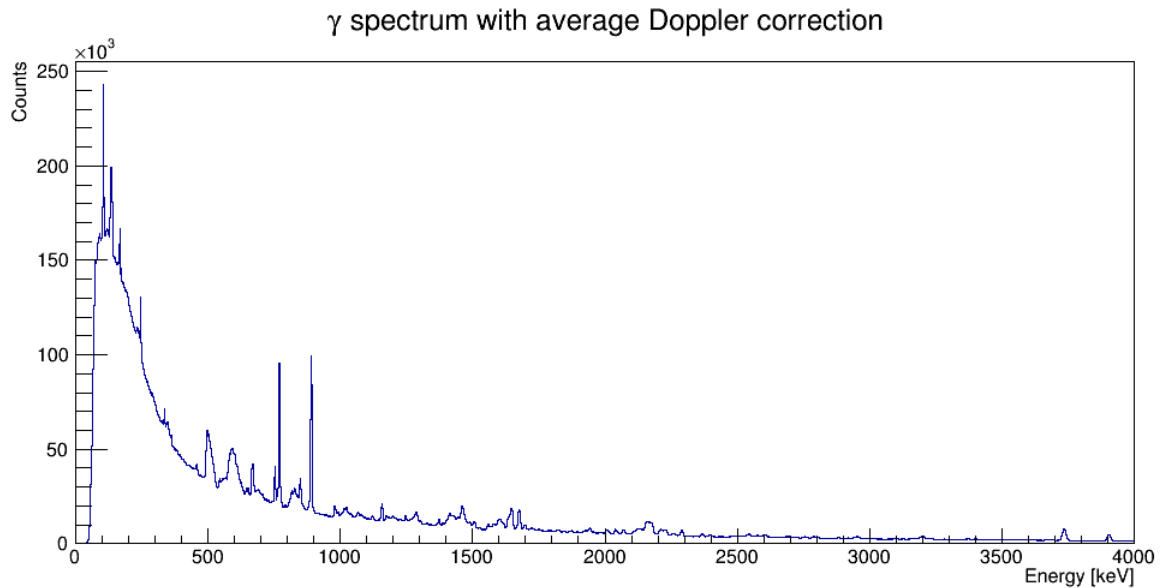
Figure 3.9: AGATA spectrum for run 3.
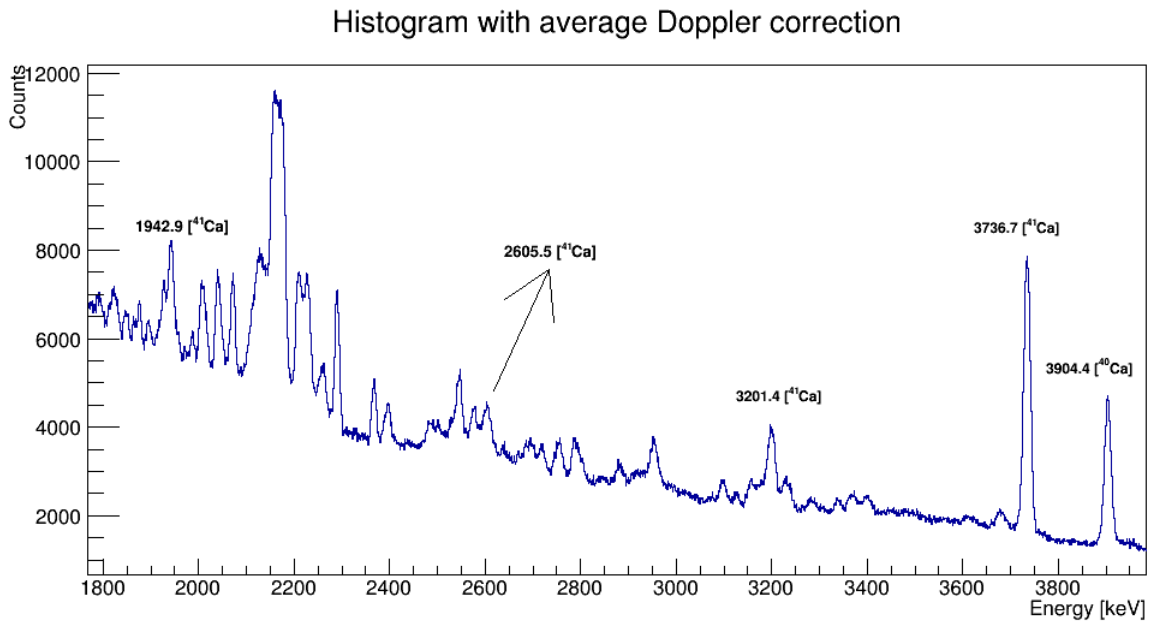
Figure 3.10: Zoom of AGATA spectrum for run 3.

The main peaks present in this spectrum are:

- 1942.9 [^{41}Ca];

- 2605.5 [^{41}Ca];

- 3201.4 [^{41}Ca];

- 3736.7 [^{41}Ca];

- 3904.4 [^{40}Ca];

In all analyzed runs, a ^{39}Ca peak was not observed because at this energy the channel with 3 neutrons evaporated is not present.

Emission of light charged particles

As introduced previously, the study of these transitions was performed in two different ways. These

two approaches will be called respectively *spectrum* approach and *projection* approach.

Within the first approach, the spectra analyzed are the ones obtained by merging the AGATA spectrum and the EUCLIDES' cuts selecting the time coincidence window.

Different coincidences of gamma-particle spectra are obtained. The next figure displays the γ spectrum in coincidence with one proton detected by at least one of the EUCLIDES' telescopes.
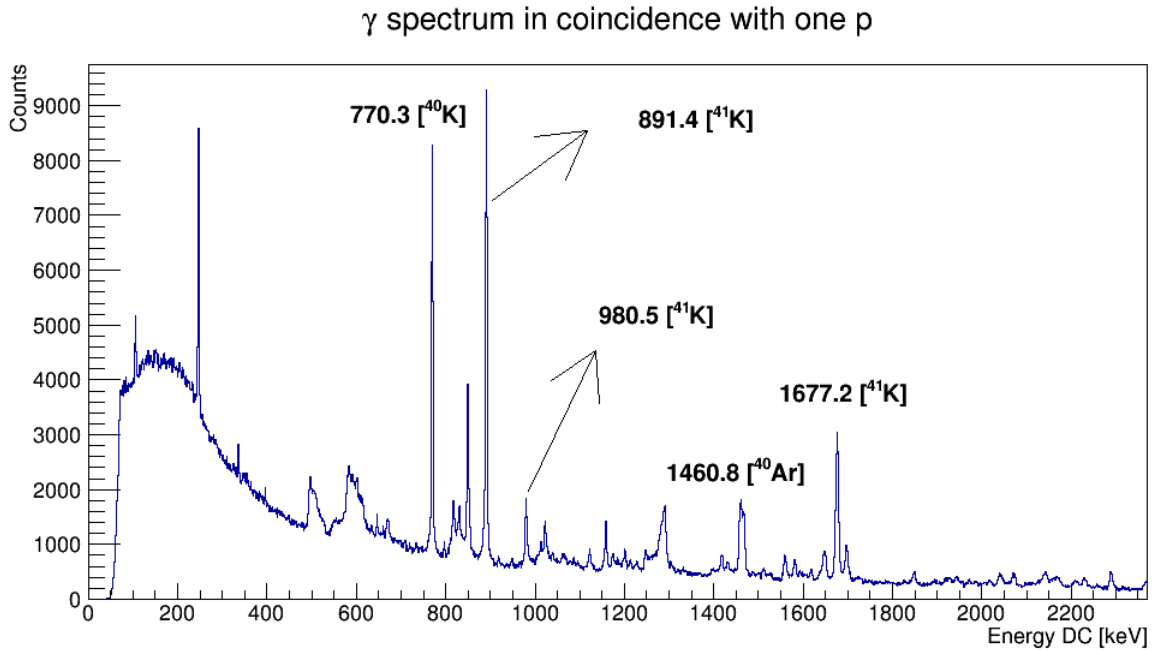
Figure 3.11: AGATA spectrum in coincidence with one proton for run 3.

The main peaks present in this spectrum are:

- 770.3 keV [^{40}K];

- 891.4 keV [^{41}K];

- 980.5 keV [^{41}K];

- 1460.8 keV [^{40}Ar];

- 1677.2 keV [^{41}K].

In one of the runs at 47 MeV one observes also the (αp) channel with the 1726.6 keV peak of the ^{37}Cl.
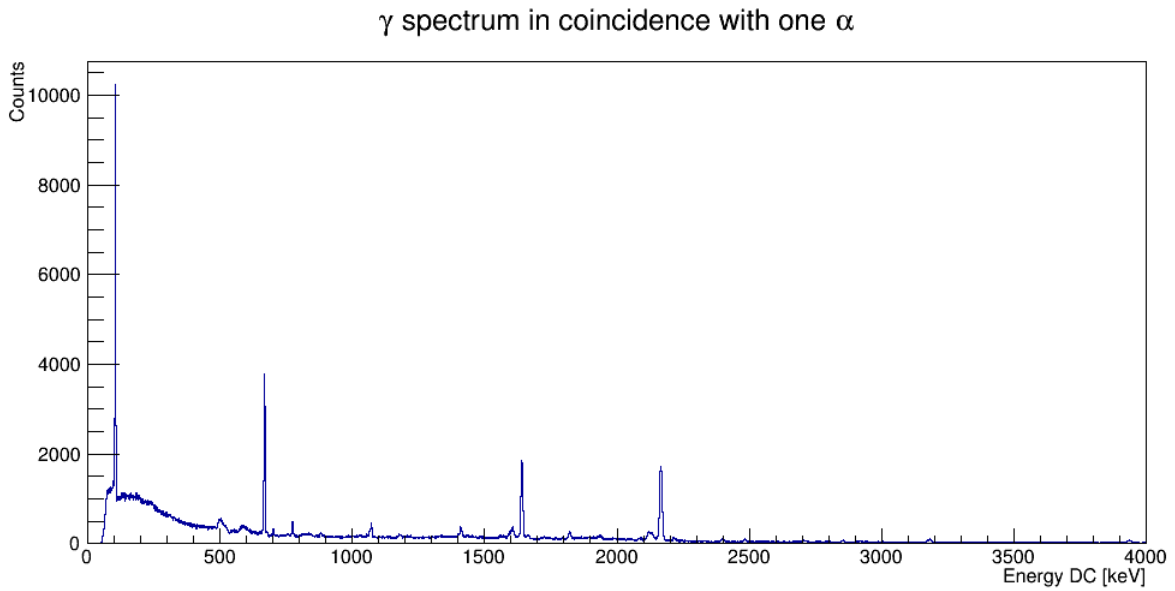
Figure 3.12: AGATA spectrum in coincidence with one α for run 3.
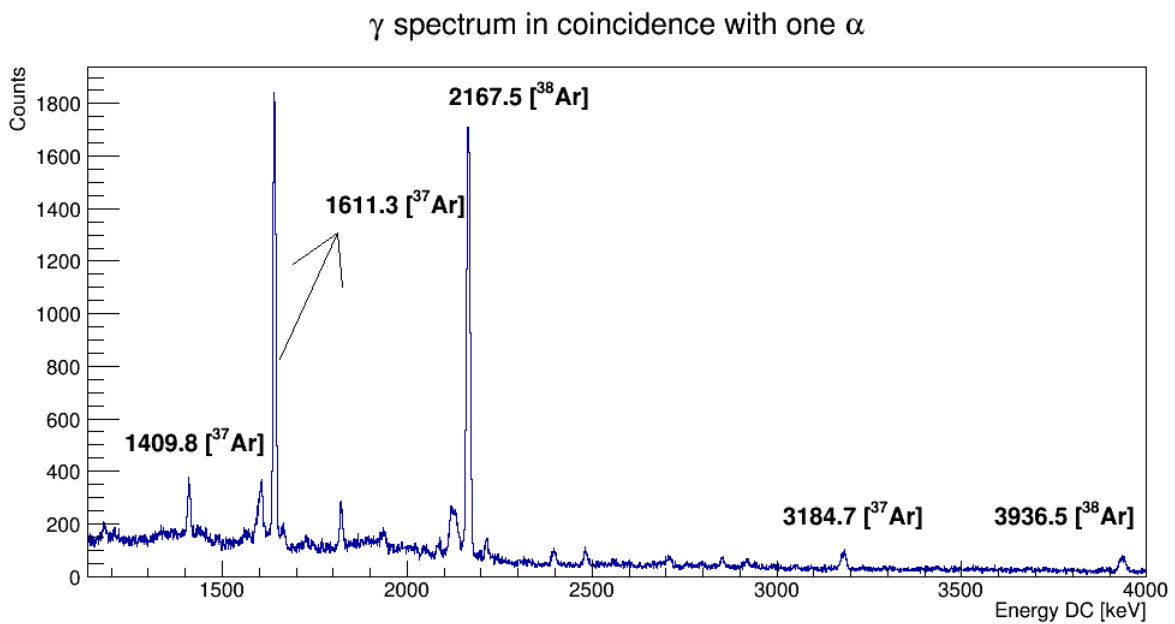
Figure 3.13: Zoom of AGATA spectrum in coincidence with one α for run 3.

Fig. 3.12 shows the γ spectrum in coincidence with a α particle detected by one of the EUCLIDES'
telescopes.
The principal peaks are:

- 1409.8 keV [^{37}Ar];

- 1611.3 keV [^{37}Ar];

- 2167.5 keV [^{38}Ar];

- 3184.7 keV [^{37}Ar];

- 3936.5 keV [^{38}Ar].
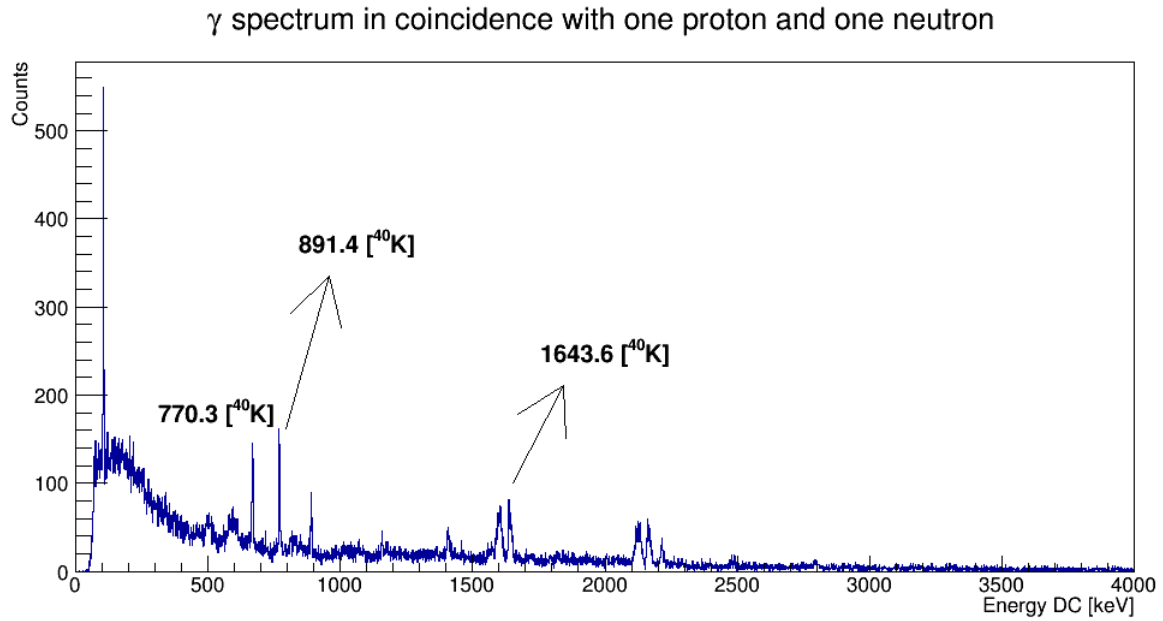
Figure 3.14: AGATA spectrum in coincidence with one proton and one neutron for run 3.

Fig. 3.14 shows a γ spectrum in coincidence with one proton and one neutron. In its analysis the main peaks to integrate are:

- 770.3 keV [^{40}K];

- 891.4 keV [^{40}K];

- 1643.6 keV [^{40}K].
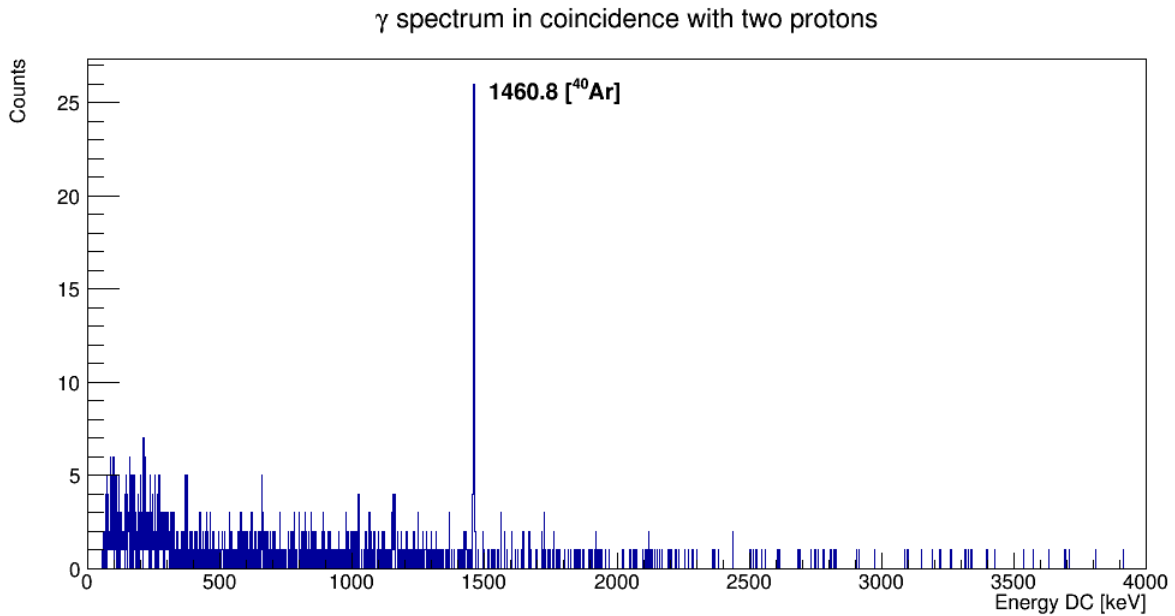
Figure 3.15: AGATA spectrum in coincidence with two protons for run 3.

Fig. 3.15 displays a γspectrum in coincidence with two protons detected by the EUCLIDES' telescopes. In this case the only relevant peak is the one at 1460.8 keV of ^{40}Ar.

Another spectrum obtained by the Selector is the one in coincidence with 2 α particles, but for all the runs no peak is visible, the entire spectrum consists of background. The analysis of these four spectra in coincidence is performed for each run. Obviously, in the runs at 40 MeV the number of counts is

lower and some peaks are not present.

The *projection* approach consists of studying the excitation energy spectrum in the function of the γ-ray energies emitted by the evaporation residues. Recalling Eq. 1.1 and Eq. 1.2 the excitation energy of the compound nucleus in the center of mass frame for this system is ∼ 27 MeV for a beam energy of 47 MeV whereas for a 40 MeV beam energy the excitation energy is around 25 MeV . The idea is to select a region of the excitation energy and project it on the γ-ray energy axis in order to obtain a spectrum as in the previous analysis. Performing this projection there is loss of statistics. Considering this aspect the projection was applied only for the runs at 47 MeV.

The maximum of the excitation spectrum is around 16 MeV. The difference between this value and the theoretical one (E_{ex} ∼ 27 MeV) is due to energy loss in the target and in the Aluminum foil in the front of the silicon detectors.

Starting from this 2D-histogram it is possible to perform the projection. The idea is to select two different energy ranges for the excitation energy. With this procedure, one obtains two spectra with different features with respect to the spectrum in Fig. 3.11. Focusing on the high-energy region in the projected spectrum the peaks related to ^{40}K are more intense with respect to the ^{41}K peaks. The reason for this lies in the fact that at higher excitation energy the compound nucleus has a higher probability of emitting more particles and not only a proton. For low excitation energy the vice versa applies. In order to understand how to select the two regions a good starting point is to plot the excitation energy in logarithmic scale.
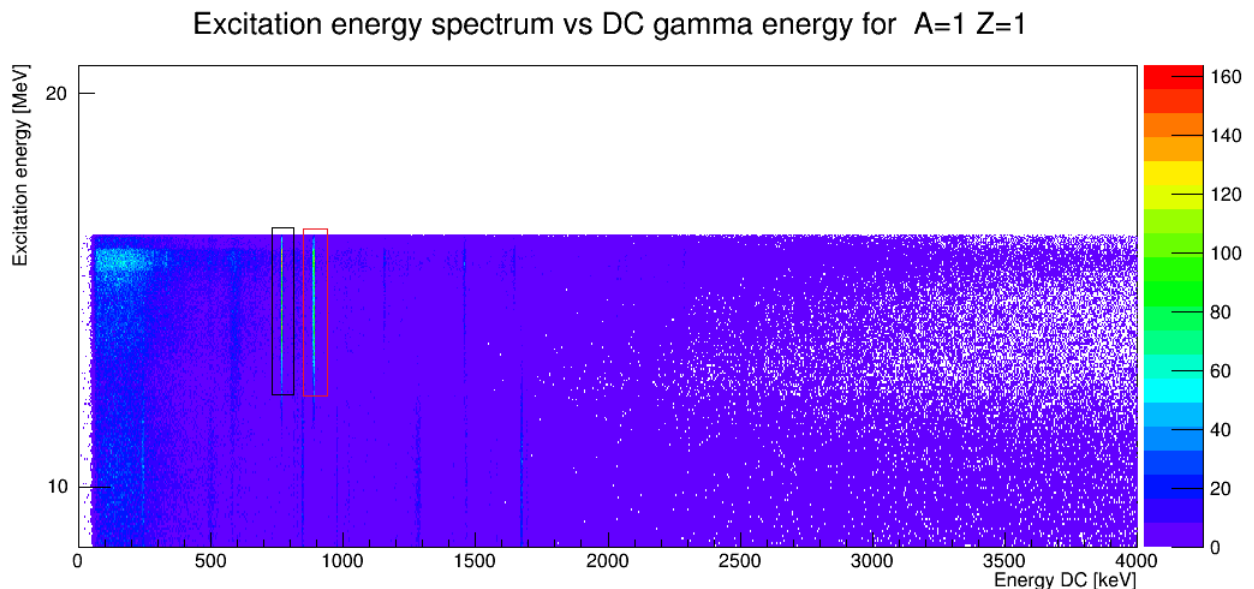
Figure 3.16: Compound nucleus excitation energy (in logarithmic scale) vs the Doppler corrected gamma energy in coincidence with one proton. In black is highlighted the 770.3 keV peak of ^{40}K and in red the 891.4 keV peak.

In the Fig. 3.16 there are two regions more intense than the others. These two regions correspond to 770.3 keV and 891.4 keV peaks of ^{40}K. Considering this aspect, the selection is made by choosing the high excitation energy region that includes these two intense peaks while the low excitation energy is chosen without the inclusion of these two intense regions.

The spectra obtained are displayed in the figure below.
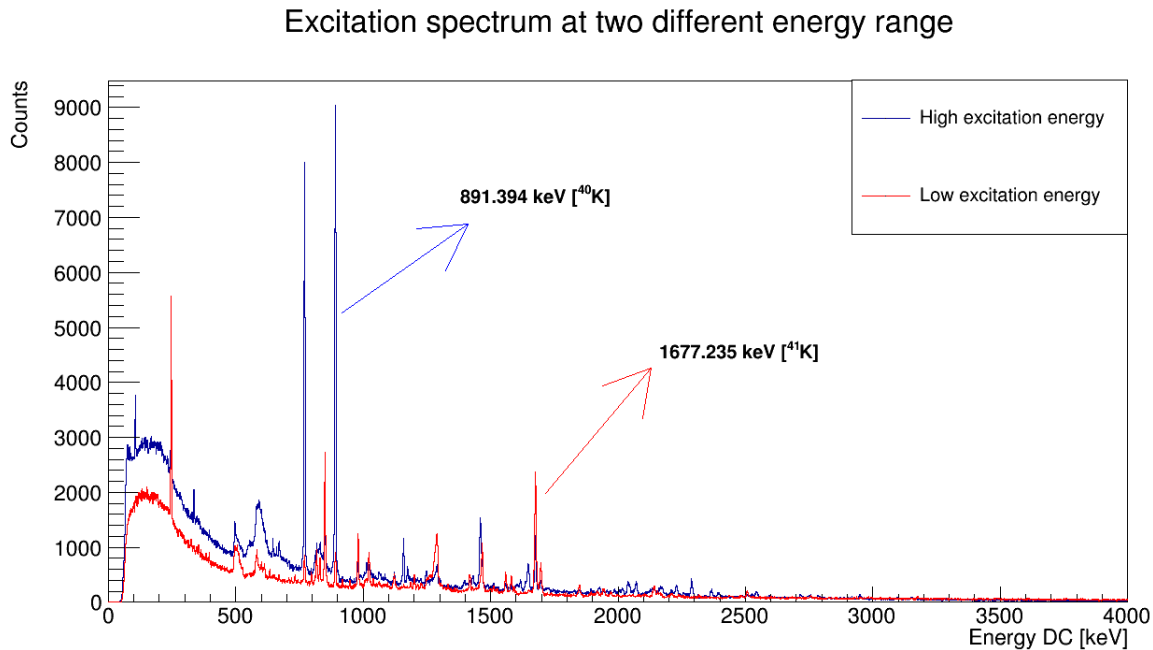
Figure 3.17: Comparison between the two spectra obtained through the projection of Fig. 3.16.

The difference between the two spectra is well visible: in blue the spectrum obtained by projecting the high excitation energy region, this can be seen by the fact that the 891.4 keV peak of ^{40}K is more intense with respect to the red spectrum. The high intensity of this peak is a clue of a high excitation energy because the compound nucleus has a higher probability of emitting more particles and so the ^{40}K peaks are more intense than the ^{41}K ones. In the red spectrum the situation is the opposite: the 1677.2 keV peak of ^{41}K is more intense with respect to the blue spectrum. This implies low excitation energy because the compound nucleus has a high probability of emitting just one proton and so the ^{41}K peaks are more intense with respect to the ^{40}K ones.

This procedure leads, from one side, to a reduction of the counts with respect to the projection approach but the great advantage is a higher simultaneous reduction of the background. This is confirmed by comparing the integral/background ratio.

Peak energy [keV]	Run 1			Run 2			Run 3		
	$(S/N)_s$	$(S/N)_p$	Ratio	$(S/N)_s$	$(S/N)_p$	Ratio	$(S/N)_s$	$(S/N)_p$	Ratio
770.3	0.27	0.35	1.30	0.20	0.43	2.15	0.22	0.52	2.36
891.4	0.24	0.32	1.33	0.15	0.36	2.4	0.2	0.76	3.8
980.5	0.012	0.06	5	0.07	0.1	1.43	0.08	0.16	2
1293.6	0.1	0.17	1.7	0.15	0.53	3.53	0.14	0.27	1.93
1559.9	0.02	0.07	3.5	0.03	0.18	6	0.16	0.25	1.56
1582.0	0.01	0.05	5	0.02	0.11	5.5	0.08	0.16	2
1677.2	0.56	0.76	1.36	0.67	0.89	1.33	0.84	1.4	1.75

Table 3.2: $(S/N)_s$ indicates the integral/background ratio in the spectrum approach while $(S/N)_p$ the same quantity but in the projection approach. 'Ratio' is the ratio between $(S/N)_p$ and $(S/N)_s$.

The Table above shows ratio values all higher than 1, so in the projection approach the background was reduced with respect to the spectrum approach.

AGATA effiency

The calculation of the efficiency is fundamental because not all the γ rays emitted by the evaporation residues can be detected by AGATA and not all the γ rays that hit a crystal are detected by

the spectrometer.

Several definitions of efficiency are present in the literature. The absolute efficiency is defined as:

$$\varepsilon_{abs} = \frac{\text{number of } \gamma \text{ detetcted}}{\text{number of } \gamma \text{ emitted by the source}} \tag{3.3}$$

while the definition of the intrinsic efficiency is:

$$\varepsilon_{int} = \frac{\text{number of } \gamma \text{ detetcted}}{\text{number of } \gamma \text{ incident on the detector}} \tag{3.4}$$

These two quantities can be related by introducing the geometric efficiency:

$$\varepsilon_{geom} = \frac{\Omega}{4\pi} \tag{3.5}$$

where Ω is the solid angle subtended by the detector.

However in the γ-ray spectroscopy field the relevant quantity is the absolute photopeak efficiency which is defined as follows:

$$\varepsilon_{photo} = \frac{\text{number of counts in the photopeak}}{\text{number of } \gamma \text{ emitted by the source}} \tag{3.6}$$

The absolute photopeak efficiency can be parametrized by the RadWare function [69] with some modifications in accordance with the experimental setup used. The expression used for the parametrization is:

$$\varepsilon_{photo}(E_\gamma) = 1.28 * \frac{30}{23} * exp\left[(A + B*x + C*x^2)^{-G} + (D + E*y + F*y^2)^{-G}\right]^{(-1/G)} \tag{3.7}$$

where x = log(E_γ(keV)/100 keV) and y = log(E_γ(keV)/1000 keV). Eq. 3.7 differs from the expression in [69] for the presence of two factors. The term 1.28 is due to the fact that the distance between the target and the edge of the ATCs is 18 cm and not 23.5 cm. The factor 30/23 takes into account that the crystals used in this experiment are 30 and not 23. The values of the parameters are reported in [70]. For sake of simplicity the expression for the error propagation is not reported.
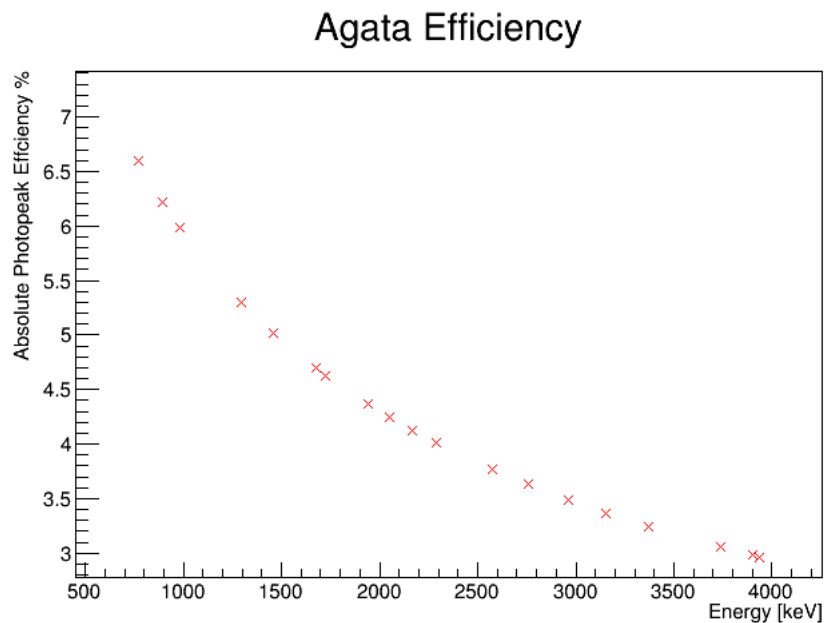

Figure 3.18: Absolute Photopeak Efficiency of AGATA calculated with Eq. 3.7 .

Energy [keV]	$\varepsilon_{photo}[\%]$
770.3	6.6 ± 0.1
891.4	6.2 ± 0.1
980.5	5.98 ± 0.09
1293.6	5.30 ± 0.09
1460.8	5.0 ± 0.1
1677.2	4.7 ± 0.1
1726.6	4.6 ± 0.1
1942.9	4.4 ± 0.1
2047.3	4.3 ± 0.1
2167.5	4.1 ± 0.1
2289.9	4.0 ± 0.1
2576.0	3.8 ± 0.1
2756.6	3.6 ± 0.2
2959.3	3.5 ± 0.2
3153.8	3.4 ± 0.2
3369.6	3.3 ± 0.2
3736.7	3.0 ± 0.2
3904.4	3.0 ± 0.2
3936.5	3.0 ± 0.2

Table 3.3: AGATA absolute photopeak efficiency.

Fig. 3.18 shows the Absolute photopeak efficiency as function of the γ-ray energy. Table 3.3 reports the values with the calculated errors.

EUCLIDES efficiency

The EUCLIDES efficiency is calculated through the ratio between the counts in the coincidence spectrum and the counts in the AGATA singles spectrum.

$$\varepsilon_{EU} = \frac{N_{coincidence}}{N_{AGATA}} \tag{3.8}$$

The error is obtained by propagation:

$$\sigma_{\varepsilon_{EU}} = \sqrt{\frac{1}{N_{AGATA}^2} * \sigma_{N_{coincidence}}^2 + \frac{N_{coincidence}^2}{N_{AGATA}^4} * \sigma_{N_{AGATA}}^2} \tag{3.9}$$

Considering that:

$$\sigma_{N_{coincidence}} = \sqrt{N_{coincidence}} \quad \text{and} \quad \sigma_{N_{AGATA}} = \sqrt{N_{AGATA}} \tag{3.10}$$

Eq. 3.9 can be rewritten as follows:

$$\sigma_{\varepsilon_{EU}} = \frac{1}{N_{AGATA}} * \sqrt{\varepsilon_{EU} * (N_{AGATA} + N_{coincidence})} \tag{3.11}$$

Peak energy [keV]	Nucleus	Run 1 ε_{EU} [%]	Run 2 ε_{EU}[%]	Run 3 ε_{EU}[%]
891.4	^{40}K	5.35 ± 0.03	10.77 ± 0.07	8.6 ± 0.04
980.5	^{41}K	11.8 ± 0.3	5.35 ± 0.03	15.4 ± 0.2
1409.8	^{37}Ar	4.6 ± 0.1	2.31 ± 0.08	5.5 ± 0.1
1460.8	^{40}Ar	7.48 ± 0.07	26.3 ± 0.3	19.0 ± 0.2
1643.6	^{40}K	2.16 ± 0.03	3.60 ± 0.07	3.13 ± 0.04
1677.2	^{41}K	5.32 ± 0.06	17.8 ± 0.2	22.3 ± 0.2
2167.5	^{38}Ar	2.86 ± 0.03	9.6 ± 0.1	8.59 ± 0.06

Table 3.4: EUCLIDES efficiency for the runs at 47 MeV.

Peak energy [keV]	Nucleus	Run 4 ε_{EU} [%]	Run 5 ε_{EU}[%]
891.4	^{40}K	4.4 ± 0.4	4.3 ± 0.2
980.5	^{41}K	5.7 ± 0.8	5.0 ± 0.2
1677.2	^{41}K	7.8 ± 0.9	12.5 ± 0.3
2167.5	^{38}Ar	2.4 ± 0.3	0.64 ± 0.01

Table 3.5: EUCLIDES efficiency for the runs at 40 MeV.

Table 3.4 and Table 3.5 are reported the results for the main peaks.

Beam Current

The beam current values are reported in [63]. They are considered without error.

Run	Energy (MeV)	I (enA)	I (pnA)	Charge state
1	47	23	3.8	6^+
2	47	//	4	6^+
3	47	35	5.8	6^+
4	40	20	4	5^+
5	40	43	7.2	6^+

Table 3.6: Beam current values for the runs analyzed.

In [63] some of the beam currents are reported in enA instead of pnA. The two quantities are related as follows:

$$I(pnA) = \frac{I(enA)}{q} \tag{3.12}$$

where q is the charge state of the ^{30}Si beam. The value for the beam current of run 1 is not present in [63], the value used is the one obtained by the Tandem database.

Duration of the runs

The duration of each run is obtained by watching the EUCLIDES timestamps, the error is set to 10%.

Run	Energy (MeV)	$\Delta t(s)$	$\sigma_{\Delta t}(s)$
1	47	30087	3008
2	47	6861	686
3	47	14244	1424
4	40	4760	476
5	40	39690	3969

Table 3.7: Duration of each run analyzed.

Target thickness

The target thickness is 0.1 mg/cm^2 and it is assumed to have the same value for all the runs. The error is set to 10%.

Target atomic mass number

The target is ^{12}C solid target, so the atomic mass number is 12.

With all this information the calculation of the fusion cross-section can be performed.

	Spectrum approach	Projection approach
Run	$\sigma_{fus}[mb]$	$\sigma_{fus}[mb]$
1	19.9 ± 0.8	19.4 ± 0.8
2	23.2 ± 0.9	22.8 ± 1.0
3	18.2 ± 0.7	18.5 ± 0.7

Table 3.8: σ_{fus} values for each run at 47 MeV.

Run	$\sigma_{fus}[mb]$
4	0.32 ± 0.03
5	0.37 ± 0.02

Table 3.9: σ_{fus} values for each run at 40 MeV.

The results for each run are reported in Table 3.8 and in Table 3.9. In order to obtain a unique value for each energy a weighted average is performed.

	Spectrum approach	Projection approach
$\sigma_{fus}[mb]$	20.0 ± 0.5	19.8 ± 0.5

Table 3.10: Weighted average of σ_{fus} at 47 MeV.

Table 3.10 reports the values obtained whereas the value at 40 MeV is:

$$\sigma_{fus} = 0.36 \pm 0.01 mb$$

These results are compared with the values obtained in [1] that are:

Energy	47 MeV	40 MeV
$\sigma_{fus}[mb]$	70.0 ± 7.2	1.4 ± 0.3

Table 3.11: σ_{fus} values obtained in [1].

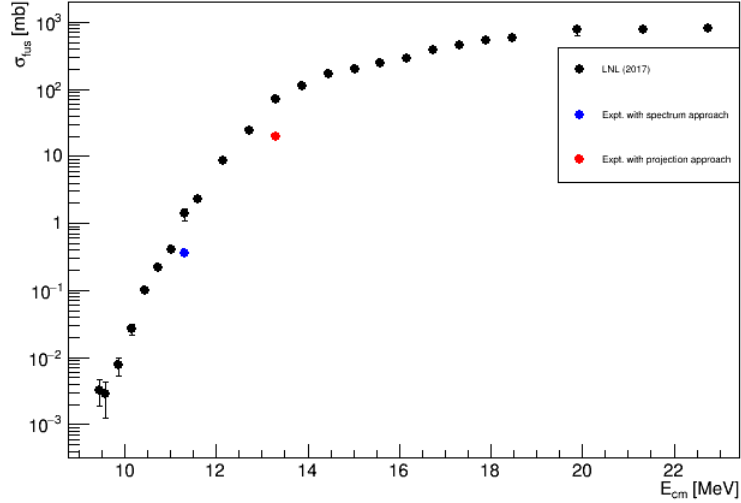The two results are not compatible as can be confirmed by the next figure.

Figure 3.19: Excitation function obtained in [1] (black points). The blue points represents the results obtained in this analysis with the spectrum approach, while in red the ones obtained through the projection approach.

However, between the values there is a discrepancy of around ~ 3.5, multiplying the values in Table 3.8 and the value of the fusion cross section at 40 MeV one obtains:

	Spectrum approach	Projection approach
$\sigma_{fus}[mb]$	70.1 ± 1.6	69.3 ± 1.6

Table 3.12: σ_{fus} values at 47 MeV considering the factor 3.5.

$$\sigma_{fus} = 1.27 \pm 0.05 \, mb$$
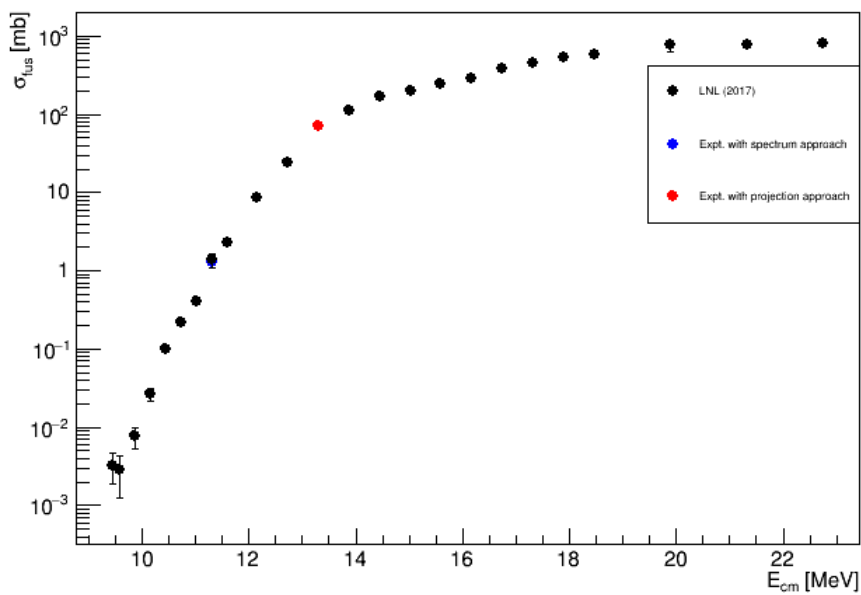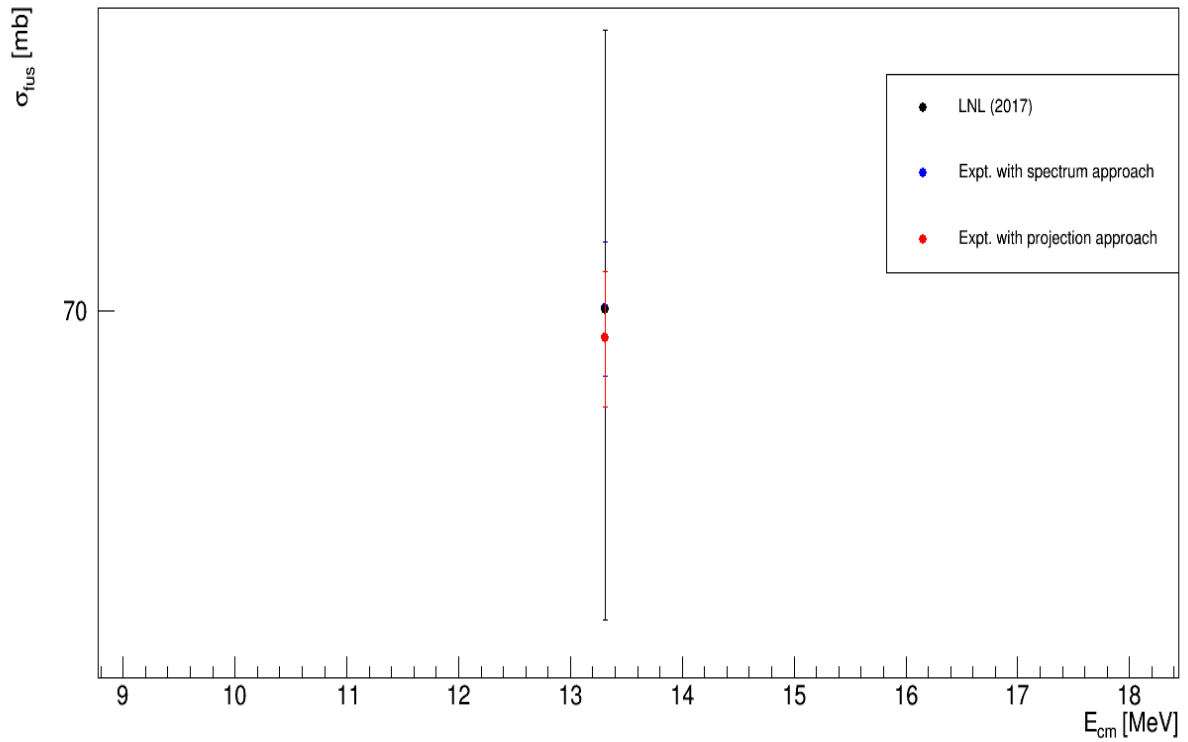
These new values follows the trend of [1].

Figure 3.20: Excitation function obtained in [1] (black points). The blue points represent the results obtained in this analysis with the spectrum approach, while in red the ones obtained through the projection approach. The factor 3.5 is considered.

Figure 3.21: Zoom on the σ_{fus} at 47 MeV
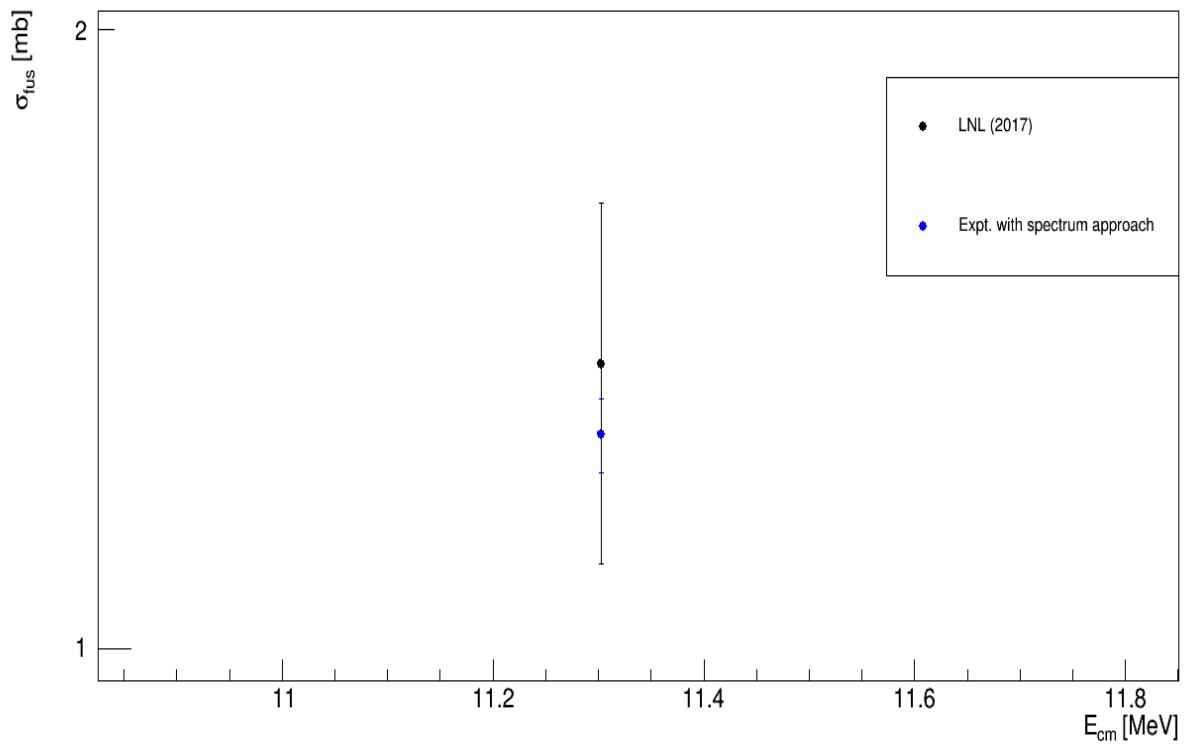
Figure 3.22: Zoom on the σ_{fus} at 40 MeV

Zooming at the 47 MeV (Fig. 3.21) and at 40 MeV (Fig. 3.22) is observed how the different values are

compatible between them also by comparing their errorbars. The factor 3.5 can be justified by some problems and limitations in the experimental setup: the geometry did not allow the use of a monitor in order to normalize the cross-section with respect to the Rutherford cross-section which accounts for the elastically scattered events. This implied that the calculation of the fusion cross-section was performed by using Eq. 3.2 where there is the value of the beam current. The problem with the beam current is that it is not constant during a run and it has large uncertainties that are difficult to be estimated.

Chapter 4

Summary and conclusions

This thesis work dealt with the data analysis of the reaction ^{12}C + ^{30}Si in inverse kinematics [71]. The fusion cross-section value was obtained for two energies. The final results are not compatible with the values obtained by precedent experiments. As pointed out previously, this can be due to some experimental problems and limitations encountered during this test. However, the purpose of the test was to study the feasibility of a cross-section measurement with the coincidence technique between γ and particles. The purpose of the test was achieved, in fact a new experiment is scheduled for November 2023. This experiment will be performed al LNL and it will investigate ^{12}C + ^{24}Mg in inverse kinematics. The experimental procedure is based on the γ-particle coincidences. In this case EUCLIDES will be replaced by two annular DSSD detectors. The separation between protons and α will not be based on the ΔE-E technique but will be performed kinematically. These detectors measure accurately the angular coordinates (θ,ϕ). A figure of one DSSD detector is shown below.
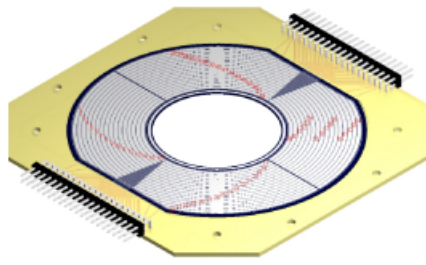

Figure 4.1: DSSD detector [71].

The experiment will have a duration of $\sim$ 10 days aiming at measuring the fusion cross-section down to about 100 nb.

Bibliography

[1] G. Montagnoli et al. "Fusion hindrance for the positive Q-value system ^{12}C + ^{30}Si". *PHYSICAL REVIEW C* 97, 024610 (2018).

[2] N. Bohr. *Nature* 137, 344 (1936).

[3] G. Montagnoli and A.M.Stefanini. *Lecture Notes heavy-Ion Reactions*.

[4] P. E. Hodgson. *Lecture at Specialist's Meeting*, Paris, 13-15 Nov. 1996.

[5] Akyüz, Ö. and A. Winther. *Proceedings of the Enrico Fermi International School of Physics* 1981.

[6] K. Hagino and N. Takigawa. *Prog.Theor.Phys.* 128 (2012).

[7] Marco Mazzocco. *Slide delle lezioni del corso Radioactivity and Nuclear Measurements* (2021-2022).

[8] .D. Landau, E.M. Lifshitz. *Quantum Mechanics: Non-Relativistic Theory* 3rd edn. (Pergamon, Oxford, 1977).

[9] D. L. Hill and J. A. Wheeler. *Phys. Rev.* 89, 1102 (1953).

[10] C. Y. Wong. *Physical Review Letters* 31, 12 (1973), pp. 766.

[11] H.Esbensen. *PRC* 77, 054608 (2008).

[12] Tomasi et al. *npa* 373 (82) 341.

[13] K. Hagino, N. Takigawa. *Progress of Theoretical Physics* Vol. 128, No. 6, 2012, p. 1061.

[14] R.G. Stokstad, Y. Eisen, S. Kaplanis, D. Pelte, U. Smilansky and I. Tserruya. *Phys. Rev. Lett.* 41, (1978) 465.

[15] M. Beckerman et al. *Physical Review Letters* 45, 18 (1980), pp. 1472.

[16] R.A. Broglia, C.H. Dasso, S. Landowne, and A. Winther. *Phys. Rev. C* 27, (1983) 2433.

[17] C.H. Dasso, S. Landowne and A. Winther. *Nucl. Phys. A* 407, 221 (1983).

[18] C.H. Dasso, S. Landowne and A. Winthert. *Nucl. Phys. A* 405, 381 (1983).

[19] C.H. Dasso, S. Landowne and A. Winther. *Nucl. Phys. A* 432, 495 (1985).

[20] G.H. Rawitscher. *Phys. Rev.* 135, B605 (1964).

[21] G.H. Rawitscher. Nucl. Phys. 85, 337 (1966).

[22] K. Hagino, N. Rowley, A.T. Kruppa. *Comp. Phys. Commun.* 123, 143 (1999).

[23] A. J. Toubiana, L. F. Canto, M. S. Hussein "Improved WKB approximation for quantum tunneling: Application to heavy ion fusion".

[24] A.T. Kruppa K. Hagino N. Rowley. *Computer Physics Communications* 123 (1999), pp. 143–152.

[25] A. B. Balantekin M. A.Nagarajan and N. Takigawa. *Phys. Rev. C* 34, 3 (1986), pp. 894–898.

[26] M. Dasgupta et al. *Annu. Rev. Nucl. Part. Sci.*, 48 (1998), pp. 401–461.

[27] C.L.Jiang, K. E. Rehm, R.V. F. Janssens, H. Esbensen et al., Phys. Rev. Lett. 93, 012701 (2004).

[28] S. Misicu, H. Esbensen. *Phys. Rev. Lett.* 96, 112701 (2006).

[29] S. Misicu, H. Esbensen. *Phys. Rev. C* 75, 034606 (2007).

[30] C. Simenel, A.S. Umar, K. Godbey, M. Dasgupta, D.J. Hinde. *Phys. Rev. C* 95, 031601(R) (2017).

[31] . T. Ichikawa, K. Hagino, A. Iwamoto. *Phys. Rev. C* 75, 057603 (2007).

[32] T. Ichikawa, K. Hagino, A. Iwamoto. *Phys. Rev. Lett.* 103, 202701 (2009).

[33] T. Ichikawa. *Phys. Rev. C* 92, 064604 (2015).

[34] T. Ichikawa, K. Matsuyanagi. *Phys. Rev. C* 88, 011602 (2013).

[35] T. Ichikawa, K. Matsuyanagi. *Phys. Rev. C* 92, 021602(R) (2015).

[36] C. L. Jiang, B. B. Back, K. E. Rehm, K. Hagino, G. Montagnoli, A. M. Stefanini. *Eur. Phys. Journ. A*, Vol. 57, 2021, p. 235.

[37] E. Margaret Burbidge, G.R. Burbidge, A.William Fowler, F. Hoyle. *Rev. Mod. Phys.* 29, 547 (1957).

[38] C L Jiang, H Esbensen, K E Rehm, B B Back, R V F Janssens, J a Caggiano, P Collon, J Greene, a M Heinz, D J Henderson, I Nishinaka, T O Pennington, and D Seweryniak. "Unexpected behavior of heavy-ion fusion cross sections at extreme sub-barrier energies". *Phys. Rev. Lett.*, 89(5):052701, 2002.

[39] C.L. Jiang, H. Esbensen, B.B. Back, R.V.F. Janssens, K.E. Rehm. *Phys. Rev. C* 69, 014604 (2004).

[40] A.M. Stefanini et al. *Phys. Rev. C* 82, 014614 (2010).

[41] C.L. Jiang. *EPJ Web of Conferences*, Vol. 17, 2011, p. 01002.

[42] C. L. Jiang, K. E. Rehm, B. B. Back and R. V. F. Janssens. *Phys. Rev. C* 79, 044601 (2009).

[43] G. Montagnoli et al. *Physical Review C* 97, 2 (2018), pp. 1–6.

[44] G. Hulke et al. *Z. Phys. A* 297, 161 (1980).

[45] S.C. Wu et al. *Nucl. Phys. A* 422, 373 (1984).

[46] S.C. Wu, Ph. D. Thesis, California Institute of Technology (1978).

[47] H. Spinka et al. *Nucl. Phys. A* 233, 456 (1974).

[48] J. Thomas et al. *Phys. Rev. C* 31, 1980 (1985).

[49] P.R. Christensen, Z.E. Switkowski. *Nucl. Phys. A* 280, 205 (1977).

[50] W. Tan et al. *Phys. Rev. Lett. C* 124, 192702 (2020).

[51] G. Fruet et al. *Phys. Rev. Lett.* 124, 192701 (2020).

[52] J.R. Patterson, H. Winkler, C.S. Zaidins. *Astrophys. J.* 157, 367 (1969).

[53] . M. Mazarakis, W.E. Stephens. *Phys. Rev. C* 7, 1280 (1973)

[54] M.D. High, B. Cujec. *Nucl. Phys. A* 282, 181 (1977).

[55] C.L.Jiang et al. *Physics review letters* 113, 022701 (2014).

[56] G. Montagnoli et al. *Phys. Rev. C* 101, 044608 (2020).

[57] Omorjit Singh Khwairakpam. Master degree thesis, "Study of tunneling effect in Nuclear Physics through the measurement of heavy ion fusion; consequences for astrophysics", Università degli studi di Padova, 2019.

[58] https://www.lnl.infn.it/tandem/.

[59] O. Klein and Y. Nishina. "Uber die streuung von strahlung durch freie elektronen nach ¨ der neuen relativistischen quantendynamik von Dirac". *Zeitschrift fur Physik* 52, 853 (1929).

[60] D. Bazzacco, "The Advanced Gamma Ray Tracking Array AGATA". *Nuclear Physics A* (2004), volume 746, p. 248.

[61] A. Wiens, H. Hess, B. Birkenbach, B. Bruyneel, J. Eberth, D. Lersch, G. Pascovici, P. Reiter and H. G. Thomas. "The AGATA triple cluster detector". *Nuclear Instruments and Methods in Physics Research A* 618, 223 (2010).

[62]] S. Akkoyun et al. "AGATA-Advanced GAmma Tracking Array". *Nuclear Instruments and Methods in Physics Research A*, 668:26–58, March 2012.

[63] https://gal-serv.lnl.infn.it:20443/exp_22.02/page-1?mod..

[64] P.A.Soderström et al. "Interaction position resolution simulations and in-beam measurements of the AGATA HPGe detectors". *Nuclear Instruments and Methods in Physics Research A*, 638:96–109, 2011.

[65]] L. Lewandowski et al. "Pulse-Shape Analysis and position resolution in highly segmented HPGe AGATA detectors". *European Physical Journal.*

[66] F. C. L. Crespi, F. Camera, O. Wieland et al. "A pulse shape analysis algorithm for HPGe detectors". *Nuclear Instruments and Methods in Physics Research A* 570, 459 (2007).

[67] D. Testov, D. Mengoni, A. Goasduff et al. "The 4π highly-efficient light-charged particle detector EUCLIDES, installed at the GALILEO array for in-beam γ-ray spectroscopy". *Eur. Phys. J. A* 55 (2019), no. 47.

[68] Locatelli Beatrice. Bachelor Degree thesis, "Misure in coincidenza di particelle e raggi γ con i set-up combinati di AGATA ed EUCLIDES per lo studio della fusione tra ioni leggeri ad energie di interesse astrofisico", Università degli studi di Padova 2022.

[69] D.C. Radfore. ESCL8R and LEVIT8R: Software for interactive graphical analysis of HPGe coincidence data sets. *Nuclear Instruments and Methods in Physics Research A*, 1995.

[70] Filippo Angelini, Master degree thesis Commissioning of the AGATA gamma-ray tracking array, Università degli studi Padova 2022.

[71] M. Del Fabbro et al., The fusion dynamics far below the barrier for ^{12}C + ^{24}Mg by γ-particle coincidences with AGATA+Si-detectors (a proposal for the XTU Tandem accelerator - June 2023).